Biomass Conversion and Biorefinery
https://doi.org/10.1007/s13399-023-04679-8

ORIGINAL ARTICLE

Phyto-mediated synthesis of pure phase α-Bi_2O_3 nanostructures using *Rubus ellipticus* plant extract: photocatalytic activity and antimicrobial efficacy

Ankush Chauhan[1,2] · Ritesh Verma[3] · Jyoti Dhatwalia[4] · Amita Kumari[5] · Vishal Dutta[6] · Gopalakrishnan Chandrasekaran[7] · Suresh Ghotekar[8] · Manpreet Kaur[9] · Janani Vignesh[7] · Shabnam Thakur[10]

Received: 12 April 2023 / Revised: 17 July 2023 / Accepted: 23 July 2023

Abstract

Bismuth-based nanoparticles are promising and widely employed in environmental cleanup. Eco-friendly Bi-based nanoparticle synthesis is being explored for nanoscale fabrication. In this study, we report on the green fabrication of alpha bismuth oxide nanoparticles (α-Bi_2O_3 NPs) using an extract from the Himalayan plant *Rubus ellipticus*. α-Bi_2O_3 nanoparticles were fabricated using methanol extract of the fruits (REF-NPs) and leaves (REL-NPs) of *Rubus ellipticus*. The optimal synthesis of α-Bi_2O_3 NPs was evaluated through X-ray Diffraction (XRD), Fourier transform infrared spectroscopy (FTIR), field emission scanning electron microscope (FE-SEM), high-resolution transmission electron microscope (HR-TEM), UV-vis spectroscopy, and X-ray photoelectron spectroscopy (XPS) techniques for crystal structure, shape, and optical characteristics. The visible light photocatalytic degradation of toxic dye-Congo red using REF-NPs and REL-NPs was performed. The photocatalytic activity of the synthesized NPs was estimated to be in order of REL-NPs > REF-NPs, with photo-degradation efficiencies of 89.2% and 84.2%, respectively, for Congo red. REL-NPs exhibited the highest rate, which was found to be 1.4 times higher than the REF-NPs sample. Photodegradation experiments revealed that the fabricated α-Bi_2O_3 exhibits enhanced degradation performance for toxic Congo red dye. The antimicrobial efficacy of REL-NPs and REF-NPs against Gram-positive (*S. aureus* and *B. subtilis*) and Gram-negative (*E. coli*, *K. pneumoniae*, and *P. aeruginosa*) bacteria, was determined. This work presents a simple green method for producing innovative α-Bi_2O_3 as a remarkable nanomaterial for aquatic bodies to break down dangerous pollutants by visible light photodegradation and as an antibacterial agent.

Keywords α-Bi_2O_3 nanoparticles · Green synthesis · Antimicrobial · Visible light photocatalysis

✉ Ankush Chauhan
ankushchauhan18@gmail.com

[1] Faculty of Allied Health Sciences, Chettinad Hospital and Research Institute, Chettinad Academy of Research and Education, Kelambakkam, Tamil Nadu 603103, India

[2] Centre for Herbal Pharmacology and Environmental Sustainability, Chettinad Hospital and Research Institute, Chettinad Academy of Research and Education, Kelambakkam, Tamil Nadu 603103, India

[3] Department of Physics, Amity University, Gurugram, Haryana 122413, India

[4] Department of Botany, Shri Sai University, Palampur, Kangra, Himachal Pradesh 176081, India

[5] Patanjali Herbal Research Department, Patanjali Research,Institute, Haridwar, Uttarakhand 249405, India

[6] University Centre for Research and Development, Department of Chemistry, Chandigarh University, Gharuan, Mohali, Punjab, India

[7] Department of Physics and Nanotechnology, SRMIST, Kattankulathur, Tamil Nadu 603203, India

[8] Department of Chemistry, Smt. Devkiba Mohansinhji Chauhan College of Commerce and Science, University of Mumbai, Dadra and Nagar Haveli (UT), Silvassa 396230, India

[9] Central Instrumentation Facility, Lovely Professional, University, Phagwara, Punjab 144402, India

[10] School of Biological and Environmental Sciences, Shoolini University of Biotechnology & Management Sciences, (HP), Bajhol-Solan -173212, India

Published online: 07 August 2023

1 Introduction

Nowadays, people are more susceptible to harmful microbes and high pollution levels because of the population boom and continual modifications in daily life [1, 2]. Additionally, the overuse and abuse of antibiotics in food and medicine have increased bacteria's resistance to them [3]. The spread of contagious diseases, the cost of medical treatments, and even the death rate among the population have all increased significantly due to antibiotic resistance [4, 5]. Metal oxide nanostructures are crucial to the development of antimicrobial and environmental remediation technologies. They are flexible materials with tremendous potential for addressing pollution and fighting microbial infections due to their capacity to harness light energy for the breakdown of organic contaminants [6–8]. Furthermore, the presence of non-biodegradable dyes in drinking water and wastewater poses a severe risk to the ecosystem, and many researchers have reported the use of nanomaterials for the effective photocatalytic degradation of these dyes [9–13]. For instance, Congo red (CR), used as a coloring ingredient in many chemical industries, harms the environment when it is discharged with effluents [14]. Diverse techniques have been used to remove this persistent dye, including flocculation, adsorption, and chemical oxidation. The problem is that because the final product of the oxidation process is unstable and toxic, some strategies increase secondary pollution and reduce the efficiency of the process [15–17]. Therefore, novel antimicrobial and photocatalytic nanomaterials that may be implemented to antimicrobial surfaces, air, and water are urgently needed [18, 19].

Over the past few decades, nanotechnology has become a noteworthy, interdisciplinary research field on a global level. The unusual physicochemical features of nanoparticles (NPs) have drawn more attention to their design, manufacture, characterization, and uses [20]. Nanoparticles typically range in size from 1 to 100 nm are incredibly small particles and have entirely different features from bulk counterparts. Because of the variety in the other specific parameters, such as size, distribution, and shape, they have a larger surface-area-to-volume ratio [21]. The improved catalytic and biological properties of the NPs are the result of their larger surface area [22, 23]. Due to their extraordinary physicochemical, optical, and biological characteristics, metal oxide NPs are widely used in a variety of pharmaceutical and industrial applications [24–26].

Amidst metal oxides, Bi_2O_3 is a significant p-type semiconductor that comes in numerous polymorphs (α, β, γ, δ, and ε) of Bi_2O_3 NPs, with diverse morphologies such as nano-flowers, thin films, nanowires, nano-plates, nano-belts, and nano-rods, for environmental cleanup [27]. Bi_2O_3 has drawn a plethora of attention due to its diverse uses as a photocatalyst [28], electrodes [29], lithium-ion batteries [30], sensors [31], biological agents [32], and catalyst [33]. The creation of Bi_2O_3 NPs has been carried out using various methods, including precipitation [34], sol-gel [29], laser ablation [35], microwave-assisted [36], hydrothermal [37], and chemical reduction approach [38]. Unfortunately, these methods utilize high pressure, high temperature, and poisonous chemicals. In order to make metal oxide NPs, researchers have discovered a viable, facile, speedy, non-toxic, affordable, and environmentally benign green technique employing natural materials like bacteria, fungi, algae, and plant extracts [39–42]. There is no demand for isolation, culturing, or maintenance because the rate of NP creation is higher [43].

Rubus ellipticus is an annual plant found in the subtropical zone of the globe. Naturally, the plant maintains a variety of habitats, including mountain valleys, roadsides, hilly terrain, forests, and slopes, throughout south and south-east Asian nations [44, 45]. In the Himalayan region, its delectable edible fruits are taken raw, and the plant's fruits, leaves, and roots are vital parts of Ayurveda, traditional Chinese medicine, and many folk remedies [46–48]. Since ancient times, diverse plant portions of this species have been used to treat dysentery, diarrhea, fever, cough, constipation, wounds, colic, vomiting, uterine relaxant, and gastric trouble. Numerous pharmacologically helpful bioactive compounds (Fig. 1) with health-promoting properties have been discovered from the species [49, 50].

There have not been many reports of studies that use plant extract to produce α-Bi_2O_3 NPs. Table 1 provides a summary of certain plant extracts used for the green synthesis of α-Bi_2O_3 NPs. In the present study, we synthesized α-Bi_2O_3 NPs from *Rubus ellipticus* fruits and leaves extract using the modified solgel method. The employed method is useful for plant extracts, which have a highly acidic nature and prohibit the reduction of nanoparticles. However, the proposed method provides the reduction of a whole metal precursor and its transformation into metal oxide, along with enhancements in their photocatalytic and biological activities. The innovative aspect of this study is developing a green approach for modifying the surface morphology of α-Bi_2O_3 NPs to improve photocatalytic activity and antimicrobial efficacy. XRD, FTIR, FE-SEM, HR-TEM, UV-vis DRS, and XPS were explored to characterize the textural properties of α-Bi_2O_3 NPs. The intrinsic mechanism of photocatalytic action has been determined. Furthermore, the antibacterial activity of the α-Bi_2O_3 NPs against gram-positive and gram-negative bacteria was tested to validate their multi-functionality. Additionally, α-Bi_2O_3 NPs exhibit a broad range of antioxidant potential as well.

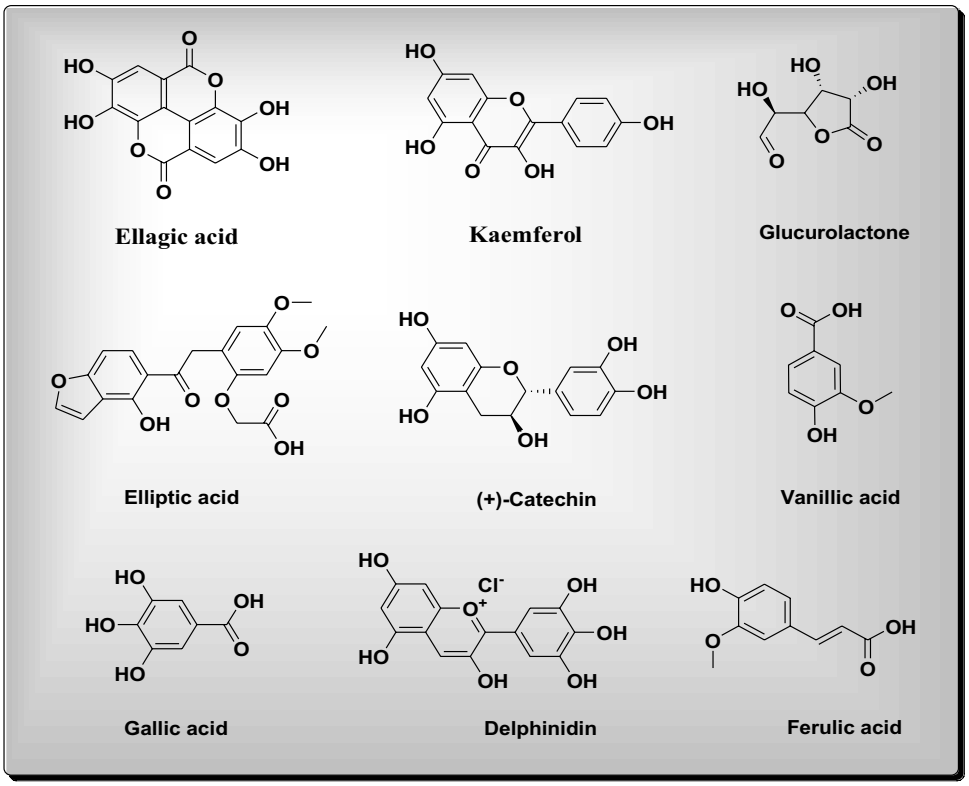

Fig. 1 Biologically active phytochemicals in *Rubus ellipticus*

Table 1 Green synthesis of α-Bi_2O_3 NPs utilizing different plant extracts

Name of the plant	Parts used	Metal precursor	Shape	Size (nm)	Ref.
Millettia pinnata	Pods	$Bi(NO_3)_3.5H_2O$	Rods & flakes	25–70	[51]
Cassia fistula	Pods	$Bi(NO_3)_3.5H_2O$	Irregular granular	63.16	[52]
Mentha Pulegium	Leaves	$Bi(NO_3)_3$	-	150	[53]
Jatropha multifida	Leaf	$Bi_5O(OH)_9(NO_3)_4$	-	17.26	[54]
Ficus benghalensis	Leaf	$Bi(NO_3)_3.5H_2O$	Rods	388	[55]
Rubus ellipticus	Fruits Leaves	$Bi(NO_3)_3.5H_2O$	Sheets Quasi-spherical	66.51 68.56	Present work

2 Experimental

2.1 Materials

The synthesis of Bi_2O_3 NPs was carried out using the chemicals bismuth nitrate pentahydrate ($Bi(NO_3)_3.5H_2O$, Sigma-Aldrich, ACS reagent, ≥98.0%), citric acid ($HOC(COOH)(CH_2COOH)_2{\cdot}H_2O$, Sigma-Aldrich, ACS reagent, ≥99.0%), polyethylene glycol ($H(OCH_2CH_2)nOH$, Sigma-Aldrich, PEG 400), deionized water (DW), methanol fruit extract, and methanol leaf extract. All chemicals were used without any purification.

2.2 Plant material collection and extract preparation

The *Rubus ellipticus* plants of the Rosaceae family were found in the district of ShimLa at an altitude of 2000, Himachal Pradesh, India. The authentication of plant material (herbarium sheets of selected plants) was done by the Botanical Survey of India (BSI), Dehradun, India, with Accession no: 117. Selected *R. ellipticus* plants' fruits and leaves were gathered in polybags and transported to the lab for analysis. The gathered produce was air dried at ambient temperature, then ground into a coarse powder

using a grinder before being kept in airtight containers. To get the coarse powers of the leaves and fruits extracts, 10 g of dried fruits/leaves samples was extracted with 100 mL of methanol in an incubator shaker for 48 h. The extracts were filtered through Whatman filter paper no. 41 and dried in a hot air oven at 37 °C, collected separately. The dried crude methanolic extracts of *R. ellipticus* fruits and leaves were further stored at 5 °C in a refrigerator for further analysis.

2.3 Fabrication of bismuth oxide nanoparticles (Bi_2O_3-NPs)

The synthesis of *Bi_2O_3-NPs* using methanol extacts of fruits and leaves of *R. ellipticus* firstly involves dissolving citric acid monohydrate 10 g in 100 mL of distilled water and 10 g of bismuth nitrate pentahydrate in 50 mL of DW in separate beakers using a magnetic stirrer. The aqueous solution of bismuth nitrate was added to the 100 mL aqueous solution of citric acid and stirred for 1 h at 60 °C. The 100 mg of dried fruit extract was dissolved in 30 mL of methanol separately and was further added to the aforementioned solutions and stirred for 30 min at 60 °C with 10 mL of polyethylene glycol (PEG). Aforementioned solution was transferred to a 500 mL round bottom flask and placed on a heating mantle for 24 h at 50 °C. The black-colored dried product was obtained, thoroughly crushed into a fine powder and calcinated at 500 °C for 5 h. The given method was employed for the synthesis of NPs using leaves extract. Finally, the yellow-colored powder was obtained, and further sent for characterization.

2.4 Characterization of fabricated nano-particles

The crystalloid structure and phase purity of the manufactured samples were verified using X-ray diffraction patterns (XRD) generated by a SmartLab 9kW rotating anode X-ray diffractometer. The surface morphology and texture of the produced NPs were investigated using high-resolution transmission electron microscopy (HRTEM, FP 5022/22-Tecnai G2 20 S-TWIN) and scanning electron microscopy (SEM, FEI-FP 5022/22-Tecnai G2 20 S-TWIN). X-ray photoelectron spectroscopy was used to probe the elemental composition (XPS, Nexsa base). Fourier transform infrared spectroscopy was used in order to detect vibrations in chemical bonds (FTIR, RZX, Perkin Elmer). Dynamic light scattering (DLS) was utilized to obtain particle size distribution and zeta potential of the nanoparticles using the Malvern Nano Zs-90 size analyzer. The UV-vis diffuse reflection spectrum was used to determine the energy bandgap and UV-vis absorption spectra of the produced NPs (UV 2450 Shimadzu).

2.5 Photocatalytic activity

To assess the photocatalytic activity of the synthesized samples, the photocatalytic degradation of Congo red in the presence of visible light was performed. In brief, a dye solution of 100 mL was prepared, and 0.05 g of photocatalyst was dispersed for the photocatalytic reaction. To achieve adsorption equilibrium, the solution was stirred in the dark for 30 min prior to the photocatalytic degradation. A halogen lamp was used as a visible light source to induce dye photodegradation, with a distance of 25–28 cm between the photocatalytic degradation solution and the light source. The catalyst was recovered by periodically collecting 5 mL of the mixture and centrifuging it at 12,000 rpm for 5 min. The maximum absorbance of the purified Congo red dye solution was determined to be at 498 nm using a UV-visible spectrophotometer. Photodegradation efficiency of the photocatalyst was calculated using the following Eq. (1) [56]:

$$\%\ \text{degradation efficiency} = \frac{C_0 - C_t}{C_0} \times 100 \quad (1)$$

where C_0 states the concentration of the initial dye solution at maximum wavelength, and C_t represents the final concentration of solution at maximum wavelength after the finishing point of the photocatalytic reaction.

2.6 Antioxidant activity (DPPH; Blois, 1958)

UV-Vis spectrophotometer readings at 517 nm were used to compare the free radical scavenging activities of REL-NPs and REF-NPs against the 2,2 diphenyl-1-picryl hydrazyl radical. The sample's activity was evaluated after being prepared in methanol at several doses (25–100 µg/mL). After adding 1 mL of DPPH reagent (0.4% DPPH in 100 mL of methanol), the absorbance was measured against a standard of ascorbic acid. The percentage of DPPH decolorization of the sample was calculated according to Eq. (2) [57]:

$$DPPH\ (\%) = \left[(Ab–Aa)/Ab\right] \times 100 \quad (2)$$

Graphs showing radical scavenging activity vs. nanoparticle concentration were constructed. Here, Ab is the absorption of the blank sample and Aa is that of the nanoparticles. The inhibitory concentration (in micrograms per milliliter, or IC50) at which 50% of DPPH radicals were scavenged is shown. The antioxidant ascorbic acid was as a reference standard.

2.7 Antimicrobial assay

The antibacterial efficacy of the synthesized samples was tested against various bacterial strains, including *Bacillus subtilis* (MTCC 441), *Staphylococcus aureus* (MTCC

737), *Escherichia coli* (MTCC 739), *Klebsiella pneumoniae* (MTCC 109), and *Pseudomonas aeruginosa* (MTCC 424). Additionally, two fungal pathogenic strains, *Fusarium oxysporum* (SR266-9) and *Rosellinia necatrix* (HG964402.1), were selected for antifungal assays. The bacterial and fungal strains were obtained from IMTech in Chandigarh and the Faculty of Biotechnology at Shoolini University in Solan, India.

2.8 Antibacterial activity

The antibacterial efficacy of REL-NPs and REF-NPs was assessed using the disc diffusion assay. Nutrient agar plates were inoculated with 100 µL of bacterial culture using sterile cotton swabs to ensure even distribution. To create a stock solution (DMSO), 50 mg of each nanoparticle type was dissolved in 1 mL of dimethyl sulfoxide. Next, 40 µL of nanoparticles was spread onto 6 mm sterilized paper discs, and the plates were incubated at 37 °C for 24 h. The size of the zone of inhibition was measured using the antibiotic zone scale once the incubation period had ended. Each antimicrobial test was repeated thrice to ensure accuracy. Ampicillin (5 mg/mL) and DMSO (solvent) were used as positive and negative controls, respectively.

2.9 Antifungal assay

The poison food method was utilized for the antifungal assay, of Dhatwalia et al. (2020) to determine antifungal activity [58]. Before usage, both the *F. oxysporum* and *R. necatrix* fungi were grown on potato dextrose agar for 7 days at 25 °C. Before pouring each plate, 24 mL of PDA was combined with 1 mL of nanoparticles (2 mg/mL). Fungal discs with a diameter of 6 mm were cut from a 7-day-old culture of both fungal strains using a flame-sterilized cork borer, then put in the middle of Petri plates and cultured at 25 °C for 7 days. On day 7 of incubation, the fungal strains were compared based on the diameter of their colonies. There were three separate tests done. The percentage inhibition was calculated by using the provided formula:

$$\text{Inhibition } (\%) = \frac{(C - T)}{C} \times 100$$

where C is the diametric growth of the colony in control, and T is the diametric growth of the nanoparticles and extract.

2.10 Minimum inhibitory concentration (MIC)

In a 96-well microtitre plate, the MIC test was used to assess the fruit extract and nanoparticles for their antibacterial and antifungal properties. Sterilized nutritional broth and potato dextrose broth were used to fill the 0.1 mL wells in each of the microtiter plate's 12 rows. To serially dilute the nanoparticles, we transferred 100 L of the test stuff from the first row to the succeeding wells in the next row of the same column, so that each well contained 100 µL of test material in serially falling concentrations. This process was repeated for wells 2 through 11. Finally, a total of 10 µL of a bacterial and fungal solution (5×10^6 CFU/mL) was applied to each well. Each plate was lightly covered with cling film to prevent the microorganisms from drying out while in culture. The deep wells were heated to 37° for 24 h. Each well was given 10 µL of a resazurin solution for use as a color indicator. A visual inspection of the well allowed us to see the color shift. The minimal effective concentration (MIC) was calculated as the concentration of extract needed to induce a detectable color change.

3 Result and discussion

3.1 XRD, FTIR, DLS, and TGA analysis

The XRD pattern of REF-NPs and REL-NPs is given in Fig. 2a, which shows the sharp peaks with high intensity, which can be related to the high crystallinity of both the prepared samples. The XRD patterns of the synthesized NPs are in good agreement with PDF card no. 71-2274 without any presence of secondary phases [59]. The diffraction peaks position in XRD plots for [REF NPs, REL NPs] and their associated (*hkl*) values are as follows [19.80, 19.83]: (110); [21.76, 21.79]: (020); [24.59, 24.62]: (−102)(021); [25.79, 25.75]: (002); [26.97, 26.94]: (−112)(111); [27.44, 27.45]: (120)(−121); [28.05, 28.07]: (012); [32.54, 32.49]: (−211); [33.07, 33.11]: (−122)(121); [33.28, 33.26]: (−202)(200); [34.02, 34.04]: (022); [35.03, 35.07]: (210); [35.43, 35.48]: (031); [35.94, 35.99]: (102); [36.99, 37.03]: (130); [37.64, 37.69]: (122); [40.09, 40.11]: (−222)(220); [41.5, 41.53]: (131); [41.92, 41.94]: (211); [42.40, 42.37]: (122). The rietveld refinement patterns shown in Fig. 2b and c were obtained using FullProf software, confirming the monoclinic phase of the synthesized α-Bi_2O_3 NPs with space group P 121/c1. The obtained lattice parameters for REF-NPs are a = 5.8463 Å, b = 8.1585 Å, c = 7.5042 Å; and REL NPs are a = 5.8434 Å, b = 8.1573 Å, c = 7.5011 Å. It can be observed that lattice parameters decreased for NPs synthesized using leaf extract with crystallite size of 66.51 nm and 68.56 nm for REF-NPs and REL-NPs. The crystallite size was calculated using Scherrer's formula given in Eq. (3) [60]:

$$d = 0.9\lambda/\beta\cos\theta \quad (3)$$

where d is the crystallite size, λ is the wavelength, β is the full-width half maxima, and θ is the diffraction angle. The

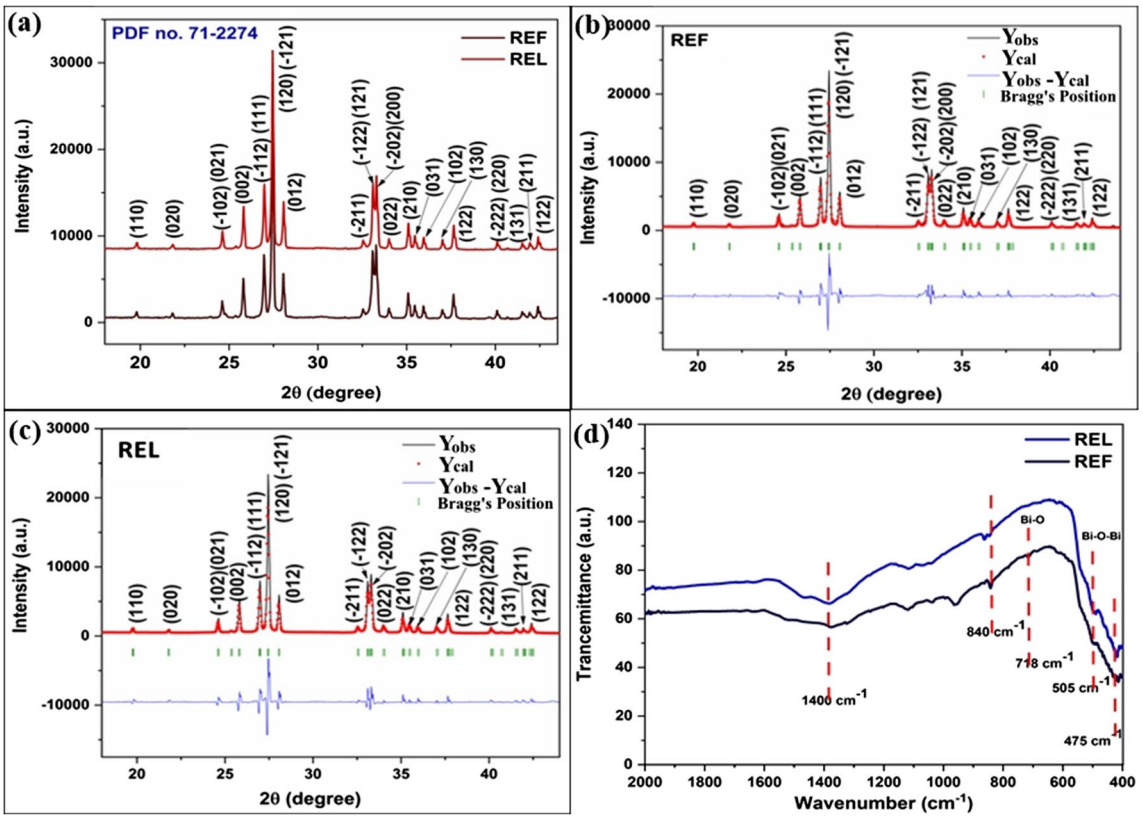

Fig. 2 **a** XRD pattern of Bi_2O_3 NPs synthesized using fruit (REF) and leaf (REL) extract; Rietveld refined patterns of **b** REF-NPs and **c** REL-NPs, **d** FTIR spectra of REF-NPs and REL-NPs

high crystallite size value can be attributed to the higher crystallinity of the samples induced due to calcination temperature. Figure 2d represents the FTIR spectra of α-Bi_2O_3 structure for REF-NPs and REL-NPs in the range of 400–4000 cm^{-1} wavenumber. In general, metal oxide semiconductor exhibits FTIR absorption bands below 1000 cm^{-1} due to the vibration of the metal-oxygen interatomic interaction. For pure α-Bi_2O_3, the broad peaks 425–510 cm^{-1} belong to the Bi-O stretching vibration of non-bonding oxygen of the distorted Bi-O polyhedral and Bi-O-Bi stretching vibration [61]. The absorption peaks at 840 cm^{-1} correspond to the monoclinic phase of the Bi_2O_3 structure [62]. The weak absorption band located at 1400 cm^{-1} can be assigned to small interlayer nitrate groups. The synthesized REF and REL Bi_2O_3 NPs in deionized water were analyzed for their size and zeta potential using dynamic light scattering (DLS) technique. The zeta potential (mV) of the synthesized REF NPs and REL NPs was measured to be −19.25 mV and −30.5 mV; the particle size distributions of the NPs are 189.46 nm and 609.43 nm. The synthesized Bi_2O_3 NPs showed excellent colloidal stability as evidenced by their narrow size distribution and high zeta potential value at room temperature.

Thermal analysis measurement of the dried precursor gel was carried using TGA and DTA. Figure 3a and b show the TGA and DTA curves of REF and REL dried precursor gel where the analysis was done in the temperature range from room temperature to 600 °C in the nitrogen atmosphere. It can be observed that the TGA curves show the weight loss in three regions at temperature around 200 °C, 310 °C, and 450 °C. The first weight loss is due to removal of water molecules content trapped inside the gel, and second major weight loss is due to the decomposition of citric acid, nitrate salts, and organic compounds present in the gel [63]. The exothermic peak can be observed at around 310 °C in DTA curve and is present due to the initiation of crystallization process which suggests that formation of Bi_2O_3 NPs initiates at this temperature. The final weight loss occurred due to phase change from unstable β-Bi_2O_3 to α-Bi_2O_3 and removal of residual impurities [64, 65].

3.2 SEM analysis

Figure 4a and b reveal the SEM micrographs of REF-NPs and REL-NPs with their EDX pattern. Figure 4a shows the self-assembly ultrathin nano-sheets to form a microsphere structure. In Fig. 4b, the REL-NPs assemble to form irregularly shaped diffused nanostructures with quasi-spherical nanoparticles.

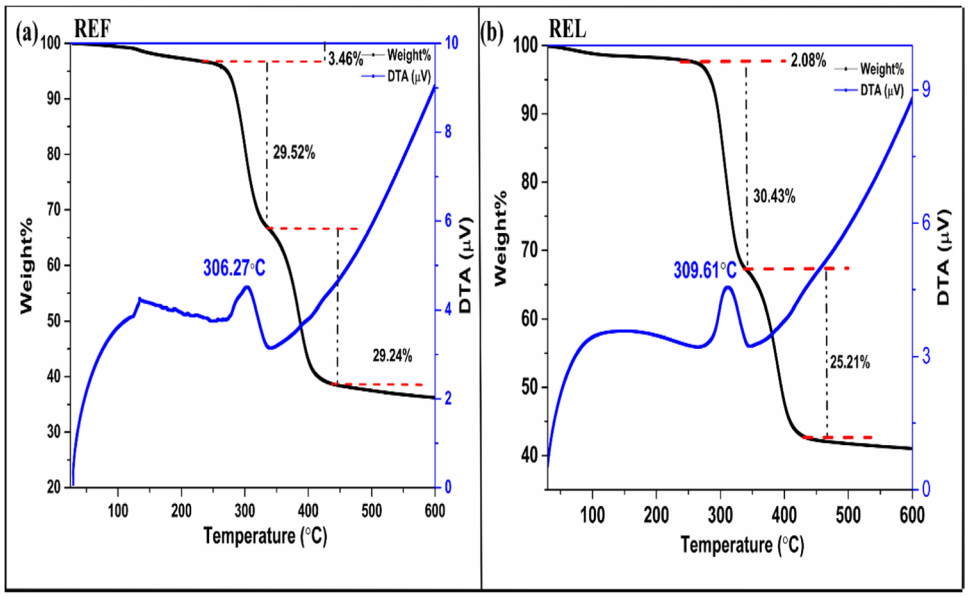

Fig. 3 TGA-DTA of **a** REF NPs and **b** REL NPs

3.3 TEM analysis

Figures 5a–d and 6a–d reveal the TEM micrographs, particle size distribution, and SAED patterns of REF-NPs and REL-NPs. Figures 5a and 6a show the self-assembly of smaller nanoparticles for bulk structures in REF-NPs and REL-NPs. The average particle size was determined using ImageJ software and plotting particle size distribution graph, which reveals the average particle size of 8.39±0.15 nm and 7.65±0.07 nm for REF-NPs and REL-NPs. In Fig. 5c and 6c, the inter-planar distance and associated (*hkl*) values were determined using the FFT function of the ImageJ software. The SAED patterns associated with REF-NPs and REL-NPs are given in Figs. 5d and 6d, which reveals that REF-NPs have high crystallinity due to sharp and bright points. At the same time, REL-NPs show scattered bright spots forming circular rings revealing polycrystalline nature.

3.4 XPS analysis

XPS measurements were performed to determine the elemental composition and binding states for the α-Bi_2O_3 NPs. Figure 7a and b show the Bi 4f core-shell spectra comprising two peaks, Bi $4f_{7/2}$ and Bi $4f_{5/2}$ [66]. The decovulation of these two peaks in Fig. 7a reveals the presence of Bi^{3+} and Bi^{2+} species in the REF-NPs. The peaks at 158.44 eV and 163.74 eV are associated with Bi^{3+} oxidation states, while peaks at 157.05 eV and 162.25 eV correspond to Bi^{2+} species [67]. It can be observed that Bi^{3+} species are dominant in REF NPs with a slight presence of Bi^{2+} species. Figure 7b reveals that the REL NPs only comprise Bi^{3+} species with associated peaks at 158.2 eV and 163.55 eV. Figure 7c and d depict the O1s spectra of REF-NPs and REL-NPs, which comprise three contributing peaks named as O_L, O_V, and O_C, corresponding to oxygen species associated with lattice of α-Bi_2O_3, oxygen vacancies, and chemisorbed oxygen species [68]. It can be observed that there is a higher percentage of the chemisorbed oxygen species associated with the REF-NPs, which in turn contributes towards enhanced photocatalytic activity and improved antimicrobial properties by providing active sites for these processes [69].

3.5 UV-visible spectroscopy

The optical properties of REF and REL α-Bi_2O_3 NPs were determined using UV-visible spectroscopy. Figure 8a shows the absorbance peak at 396 nm for REF-NPs and REL-NPs in the 200–800 nm range. The direct energy optical band gap (Eg) for REF-NPs and REL-NPs was determined using the Tau's relation (Eq. 4) [70]:

$$(\alpha h\nu)^2 = A(h\nu - Eg) \quad (4)$$

where α is the absorption coefficient and hν corresponds to the photon energy. Hence, the plot between $(\alpha h\nu)^2$ and (hν) gives the energy band gap (E_g). Figure 8b reveals the direct energy band gap of 2.8 eV for both the REF-NPs and REL-NPs, which match well with the previously reported values of Eg for α-Bi_2O_3 NPs [62, 71].

3.6 Photocatalytic studies

The photodegradation activity of biogenic samples was scrutinized by opting for a toxic dye, viz., Congo red. The dye concentration was found to drop steadily with time for both synthesized REF-NPs and REL-NPs. After 110 min of visible

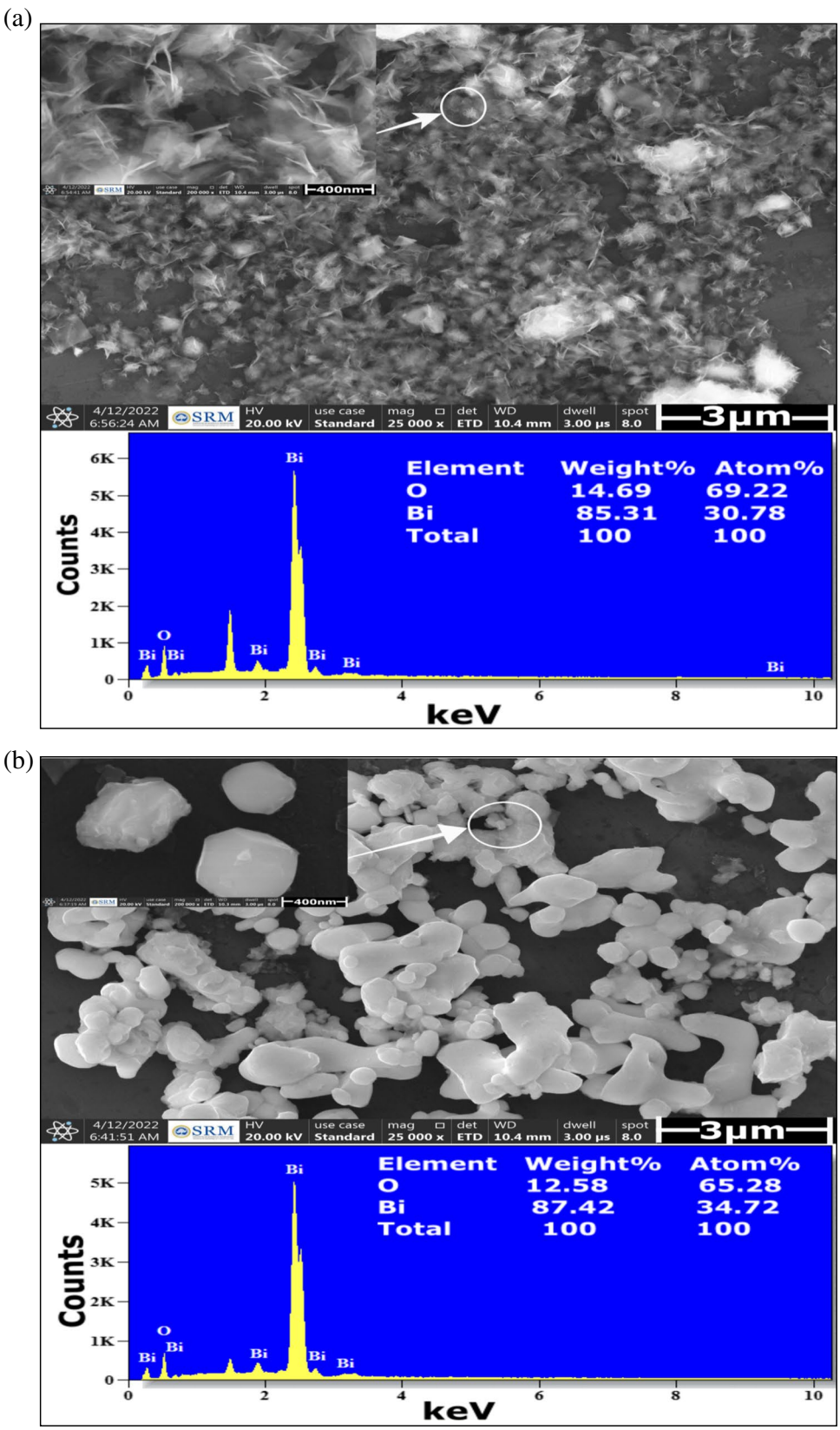

Fig. 4 **a** SEM with EDX pattern for REF-NPs. **b** SEM image with EDX pattern for REL-NPs

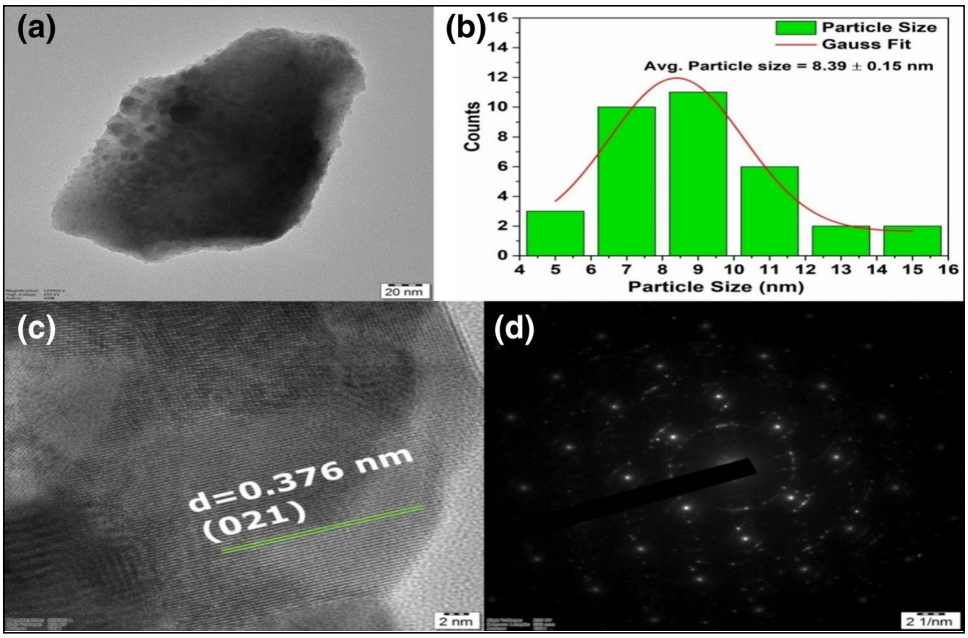

Fig. 5 **a** TEM micrograph, **b** particle size distribution, **c** interplanar distance, and **d** SAED pattern of REF-NPs

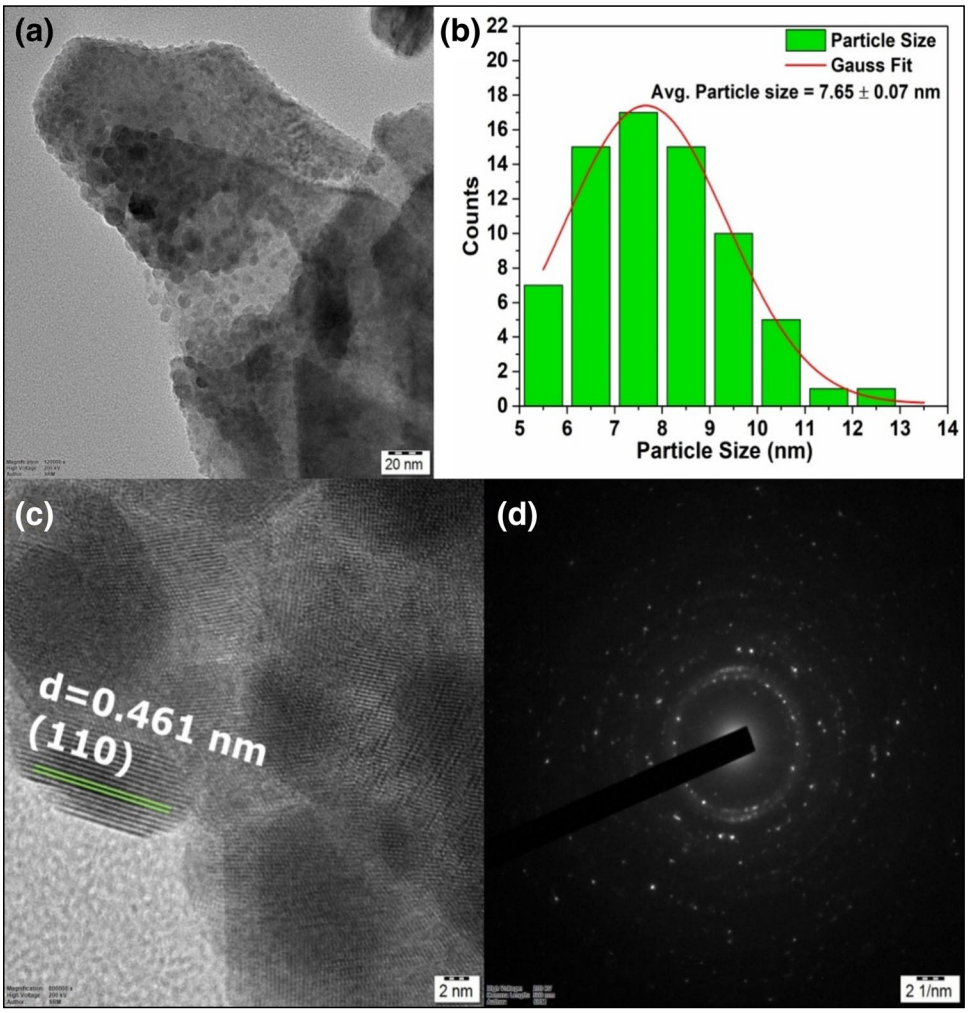

Fig. 6 **a** TEM micrograph, **b** particle size distribution, **c** interplanar distance, and **d** SAED pattern of REL-NPs

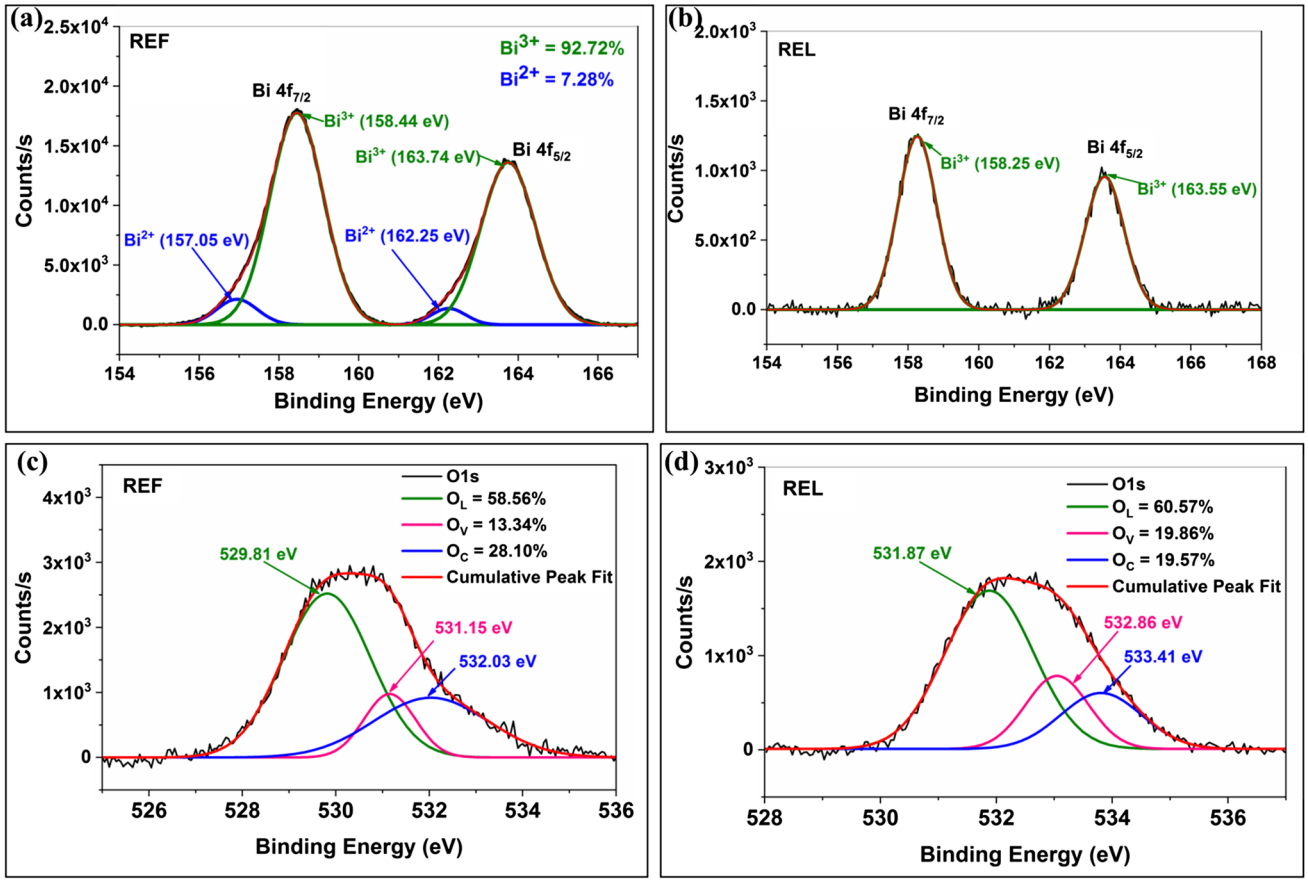

Fig. 7 Bi 4f spectra of **a** REF-NPs and **b** REL-NPs and O1s spectra **c** REF-NPs and **d** REL-NPs

light irradiation, only about 5% of the dye was found degraded without photocatalysts, exemplifying that Congo red is a highly stable dye. The absorbance of the dye solution was studied after the solution was taken from the reactor at a time interval after visible light illumination. Figure 9a and b depict the absorption spectra for both samples, such as (a) REF-NPs and (b) REL-NPs, clearly indicating the enhanced photocatalytic activity of these nano-photocatalytic semiconductors. The photocatalytic activity of all synthesized samples was estimated in the order of REF-NPs < REL-NPs with photo-degradation efficiency of

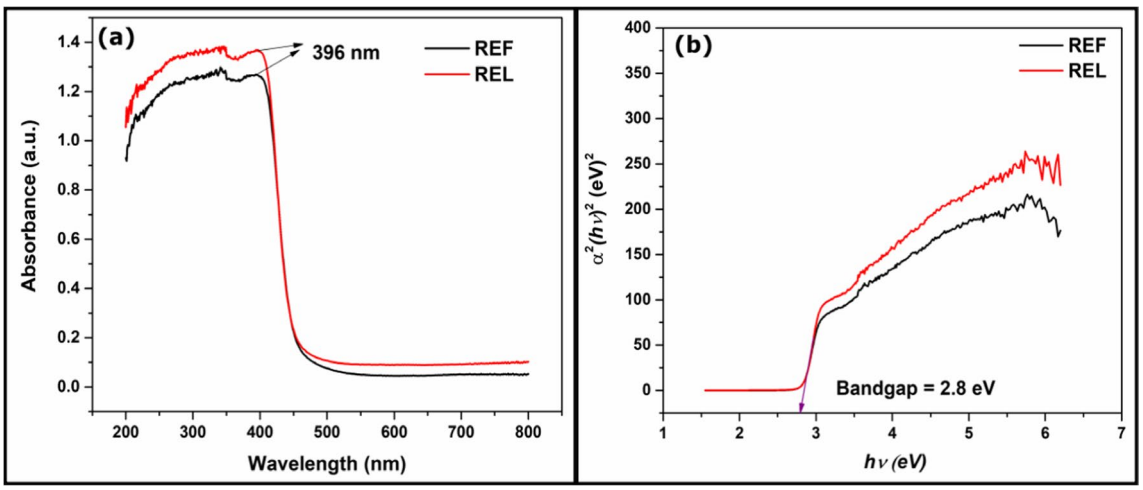

Fig. 8 **a** UV-visible absorbance spectra. **b** Direct energy bandgap (Eg) of REF-NPs and REL-NPs

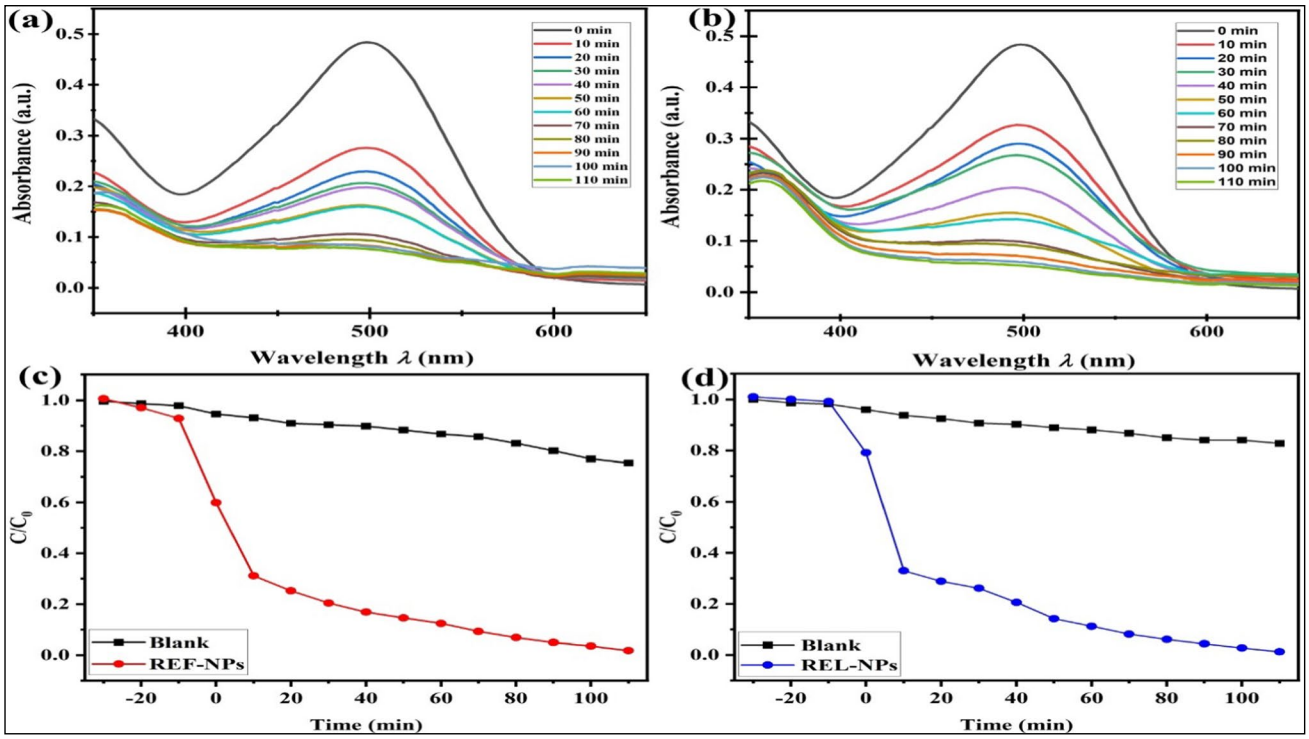

Fig. 9 Wavelength vs. absorbance graph for **a** REF-NPs and **b** REL-NPs, photocatalytic degradation of Congo red dye using sample **c** REF-NPs and **d** REL-NPs under visible light using fabricated biogenic semiconductor photocatalysts. [Reaction conditions (RC): (dye) = 1×10^{-5} mol.dm^{-3}; (fabricated sample) = 50 mg/100 mL; pH = 7 and intensity of light = 750 lx]

84.22% and 89.24%, respectively, for Congo red (Fig. 9c, d). Photo-degradation experiments revealed that the fabricated α-Bi_2O_3 owns the enhanced degradation performance for toxic Congo red dye. First pseudo order kinetics of degradation results were estimated using Eq. (5), Langmuir Hinshelwood model:

$$-\mathrm{Ln}(C/C_0) = kt \quad (5)$$

where C represents the initial and C_0 displays the final concentration of dye, respectively, at t (min), and k is the rate constant value for the degradation of Congo red dye.

The rate order obtained was estimated as 0.0010 min^{-1} for the REF-NPs sample (Fig. 10a) and 0.0014 min^{-1} for the REL-NPs sample (Fig. 10b) for the photocatalytic degradation of Congo red dye. Comparing both samples, REL-NPs exhibited the highest rate, which was found to be 1.4 times higher than the REF-NPs sample (Fig. 10c). COD and CO_2 removal experiments were carried throughout photocatalytic examination of toxic dye for both samples. As represented in Fig. 10d, REF-NPs removed 93.11% of COD, and the REL-NPs sample eliminated 99.55% of COD for photo-catalytic removal of Congo red dye. Under certain reaction parameters, the complete degradation of Congo red dye has significantly aided COD removal tests. The COD elimination results were supplemented by CO_2 approximation experiments (Fig. 10a). CO_2 production during dye degradation recommends that the degradation of Congo red dye emits CO_2 and H_2O as byproducts. The mineralization ability of the REL-NPs sample was found to be higher than that of the REF-NPs sample for photodegradation of Congo red. Aside from photocatalytic efficacy, the reusability and stability of photocatalysts are important considerations in practical research. To test the re-usability of fabricated plant extract-based samples, we ran a photocatalytic process continuously recycled for photodegradation of Congo red. After 5 cycles, there was no visible decrease in dye degradation. Thus, both fabricated samples, viz., REF-NPs and REL-NPs were discovered to be highly stable (Fig. 10b, c). According to the results of re-cyclic investigations, the fabricated REL-NPs photocatalyst sample exhibits extraordinarily high stability. We performed a control experiment with no radical scavengers to exclude the possibility of dye degradation by radical scavengers. For superoxide radicals ($\bullet O_2^-$), hydroxyl radicals (•OH), and holes (h^+), respectively, P-benzoquinone (BQ), Tert-butyl alcohol (TBA), and sodium ethylene diamine tetraacetic (Na_2-EDTA) were employed. Figure 11 illustrates scavenging tests for Congo red photo-degradation using REF-NP (Fig. 11d) and REL-NP samples (Fig. 11e). The photodegradation percentages of both samples were reduced in the presence of BQ, TBA, and Na_2-EDTA, with 52.1%, 78.4%, and 28.4% using REF-NP samples and 56.3%, 81.9%, and 32.4% using REL-NPs sample, respectively. These data revealed that superoxide and hydroxyl radicals were the predominant active

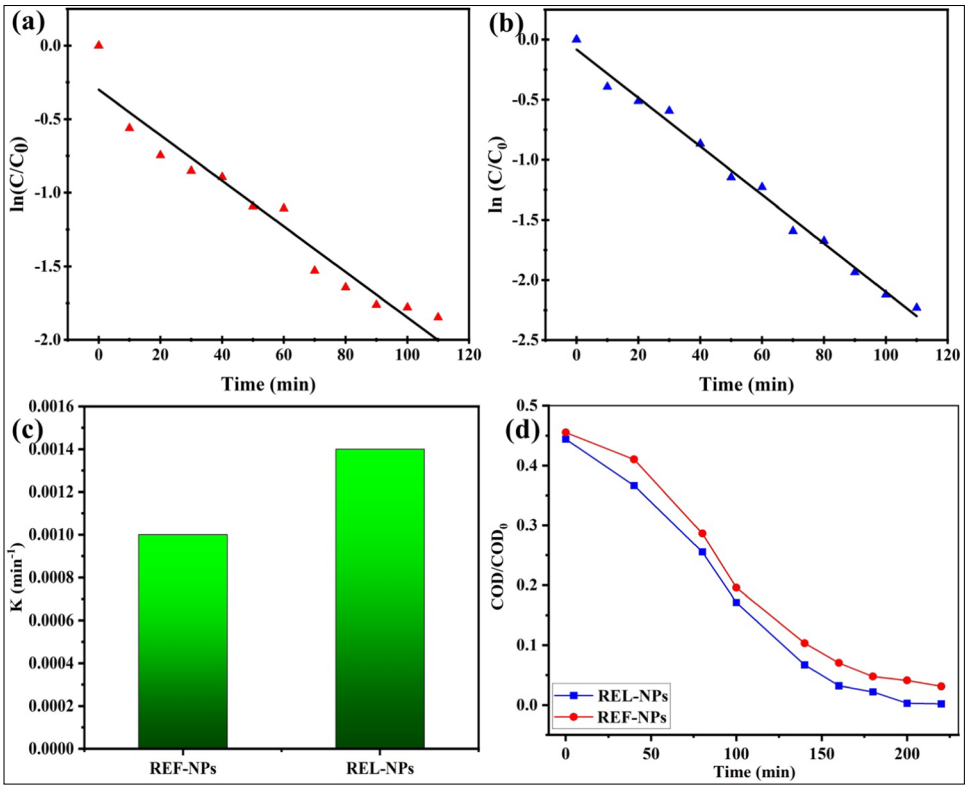

Fig. 10 First-order kinetics fitting data for photocatalytic degradation **a** REF-NPs, **b** REL-NPs, **c** rate constant value (k) for photocatalytic degradation for both samples, and **d** COD elimination using both samples. [Reaction conditions (RC): (dye) = 1 × 10–5 mol. dm–3; (fabricated sample) = 50 mg/100 mL; pH = 7 and intensity of light = 750 lx]

species in the photo-degradation of Congo red hazardous dyes in 110 min utilizing α-Bi_2O_3 under visible light.

3.7 Photocatalytic mechanism

Mulliken electronegativity theory [72] was used to determine potential band positions in order to explore the photocatalytic degradation mechanism (Eqs. (6) and (7)):

$$E(VB) = X - Ee + 0.5Eg \tag{6}$$

$$E(CB) = E(VB) - Eg \tag{7}$$

where E_e represents electron-free energy on the hydrogen scale (+4.50 eV) and E_g defines the band gap energy of the semiconductor photocatalyst. The estimated band gap of plant extracted α-Bi_2O_3 was found to be 2.8 eV for both REF-NP and REL-NP samples. The band potentials were estimated as −0.34 eV for E_{CB} and +3.14 eV for E_{VB}. The photoinduced charge-transfer mechanism is presented in Fig. 12 based on the aforementioned optical characterization, estimated energy band positions, and ROS trapping investigations, with matched band positions of synthesized α-Bi_2O_3. Under visible light, photocatalysts get stimulated, and electron-hole pairs are photogenerated; the superoxide generation will take place on the conduction band of the Bi_2O_3 as the E_{CB} position of Bi_2O_3 is enough for photo reduction O_2/O_2^{-}•. The more negative reduction potential E_{CB} of Bi_2O_3 (−0.34 eV) than the reduction potential O_2/O_2^{-}• (−0.33 eV vs. NHE) [72], the electrons at E_{CB} of Bi_2O_3 competently reduce O_2 into O_2^{-}• radicals. Then, photo-induced superoxide (O_2^{-}•) radicals oxidized the dye molecules to H_2O and CO_2. Furthermore, the E_{VB} potential of Bi_2O_3 is directly greater than the conventional redox potential of H_2O/•OH (+2.5 eV vs. NHE) [73]. As a result, the holes are capable of photoreduction of H_2O radicals to •OH radicals. Scavenging studies, on the other hand, demonstrated that O_2^{-}• and •OH were active radical species throughout the photo-degradation process. Conversely, the E_{VB} potential of Bi_2O_3 (+3.14 eV) is more favorable than the normal redox potential of H_2O/O_2 (+0.82 eV vs. NHE); thus, holes (h+) in Bi_2O_3 E_{VB} immediately react with H_2O molecules to generate O_2. Thus, photo-generated molecular oxygen-induced O_2^{-}• and then •OH contribute to enhanced photodegradation performance which was found consistent with the findings of scavenging experiments.

4 Phytochemical screening of plant extracts

The results showed the presence of phenols, tannins, terpenoids, flavonoids, saponins, and glycosides in the methanol extract of leaves and fruits of *R. ellipticus* (Table 2). Similar to the present study, Saklani et al. (2012) and Shibu Prasanth and

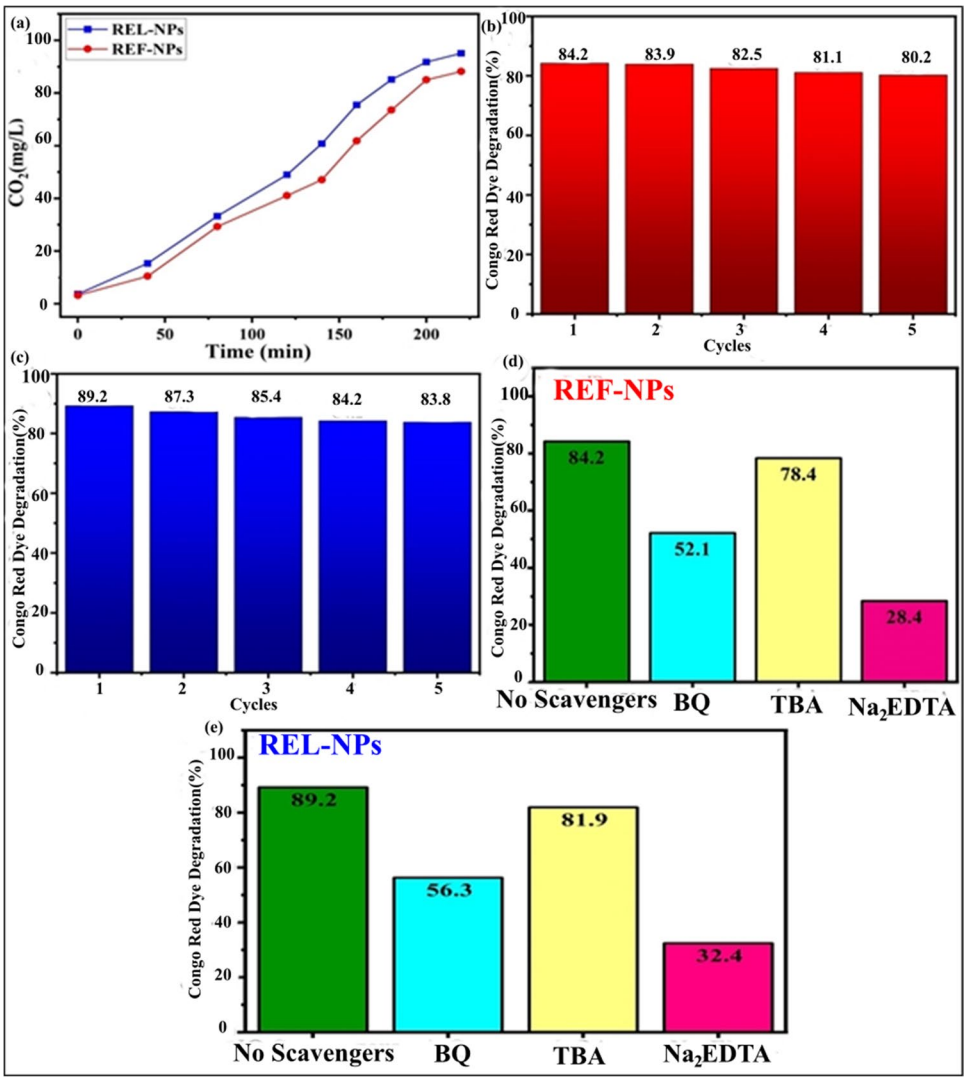

Fig. 11 **a** CO_2 approximation, reusability tests **b** REF-NPs, **c** REL-NPs and scavenging experiments **d** REF-NPs, **e** REL-NPs. [Reaction conditions (RC): (dye) = 1 × 10–5 mol. dm–3; (fabricated sample) = 50 mg/100 mL; pH = 7 and intensity of light = 750 lx]

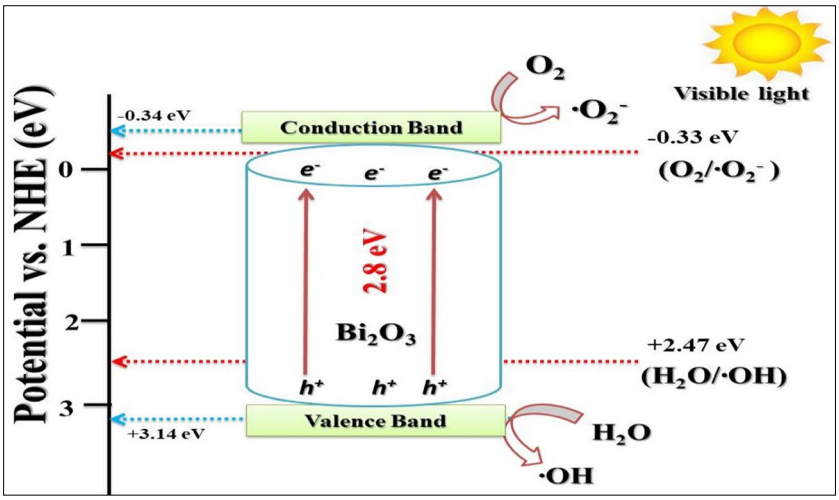

Fig. 12 Proposed possible photocatalytic mechanism using semiconductor under visible light

Table 2 Preliminary phytochemical screening of methanol extract of *R. ellipticus*

Sr. no.	Phytochemicals	Methanolic extract of leaves	Methanolic extract of fruits
1.	Phenols	+	+
2.	Tannins	+	+
3.	Glycosides	+	+
4.	Saponins	+	+
5.	Flavonoids	+	+
6.	Terpenoids	+	+

("+" presence of phytochemical)

Chandran (2017) also reported the presence of tannins, phenols, saponins, flavonoids, glycosides, terpenes, and proteins in the methanol extract of *R. ellipticus* leaves and fruits [74, 75]. The phytochemical constituents in *R. ellipticus* plants act as stabilizing agents for synthesizing bismuth oxide nanoparticles. The plant extracts act as a reducing and capping agent that reduces particle size and increases the antimicrobial activity of nanoparticles [76, 77].

4.1 Antioxidant activity

The antioxidant activity of REL-NPs and REF-NPs has presented in Fig. 13. The results indicated that as the concentration of REL-NPs, REF-NPs, and ascorbic acid (AA) increased (25–100 µg/mL), the percentage inhibition was also increased Fig. 13. At a concentration of 100 µg/mL, the maximum percentage inhibition was found to be 48.28±0.34% with REF-NPs, while the minimum inhibition was found to be 43.13±0.40% with REL-NPs. The IC_{50} value of REL-NPs, REF-NPs, and AA were observed as 130.26 µg/mL, 113.20 µg/mL, and 24.32 µg/mL, respectively. The lower IC_{50} value observed during the present study indicated the higher antioxidant activity of nanoparticles. The

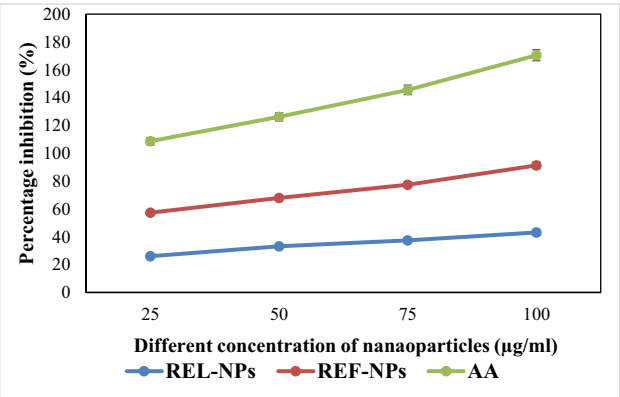

Fig. 13 Antioxidant activity of nanoparticles

REF-NPs showed higher antioxidant potential as compared to REL-NPs. A previous study also discussed the antioxidant activity of bismuth oxide nanoparticles from the *Delftia* species with an IC_{50} value of 307 µg/mL [78]. Similarly, Das et al. also reported that the metallic bismuth nanoparticles were prepared from leaves extracts of *Moringa oleifera* and showed good antioxidant activity [79].

4.2 Antimicrobial assay

4.2.1 Antibacterial activity

REL-NPs and REF-NPs produced from the aqueous extract of *R. ellipticus* were evaluated against Gram-positive (*S. aureus* and *B. subtilis*) and Gram-negative (*E. coli*, *K. pneumoniae*, and *P. aeruginosa*) bacteria for their antibacterial activity. The results of the disc diffusion assay and MIC assay are presented in Figs. 14 and 15. The nanoparticles showed higher antibacterial activity against Gram-positive bacteria than Gram-negative bacteria. The REL-NPs showed maximum zone of inhibition and MIC value against *S. aureus* (16.66±1.0 mm; 250 µg/mL) and *B. subtilis* (16±1.0 mm; 250 µg/mL) followed by *E. coli* (13±1.0 mm; 500 µg/mL), *P. aeruginosa* (12.6±0.5 mm; 1000 µg/mL), and *K. pneumonia* (10.6±0.5 mm; 1000 µg/mL). The REF-NPs revealed the maximum antibacterial activity against *S. aureus* and *B. subtilis* (125 µg/mL) than the remaining strains of bacteria (500 µg/mL). In comparison to both nanoparticles, REF-NPs showed higher antibacterial potential than REL-NPs. The antibacterial activity varies with the concentration, surface area, morphology, and crystalline nature of the nanoparticles [80]. The present study results were similar to the results of Jassim et al. and Motakef-Kazemi and Yaqoubi et al. who investigated the antibacterial activity of bismuth oxide nanoparticles against *E. coli*, *P. aeruginosa*, *S. aureus*, and *Salmonella typhi* [53, 81]. Similarly, Das et al. also reported the good antibacterial potential of *Moringa oleifera* leaves extract-mediated metallic bismuth nanoparticles against Gram-positive and Gram-negative bacteria. The difference between Gram-positive and Gram-negative bacteria may be due to the cell wall structure, physiology, and cell surface receptors [79].

4.2.2 Antifungal activity

Using the food poison approach and the minimum inhibitory concentration (MIC) method, the antifungal activity of REL-NPs and REF-NPs was assessed for two fungal strains (*F. oxysporum* and *R. necatrix*), and the findings are shown in Figs. 16 and 17. The REL-NPs showed the maximum inhibition of *R. nectatrix* (58.0±0.6%; 250 µg/mL) and then *F. oxysporum* (52.2±1.0%; 500 µg/mL). Similarly, REF-NPs also showed higher antifungal activity against *R. nectatrix*

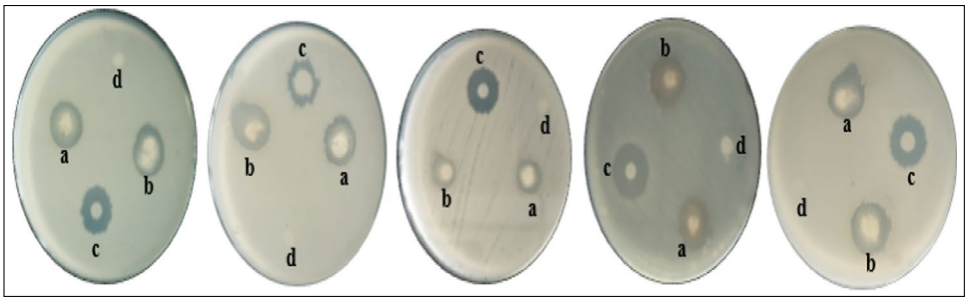

Fig. 14 Petri plats showing zone of inhibition of REL-NPs and REF-NPs against *E. coli* (A), *P. aeruginosa* (B), *K. pneumoniae* (C), *B. subtilis* (D), *S. aureus* (E). Here, a REL-NPs (2 mg/mL), b REF-NPs (2 mg/mL), c positive control (Amp: 50 µg/mL), d negative control (DMSO 10 µL)

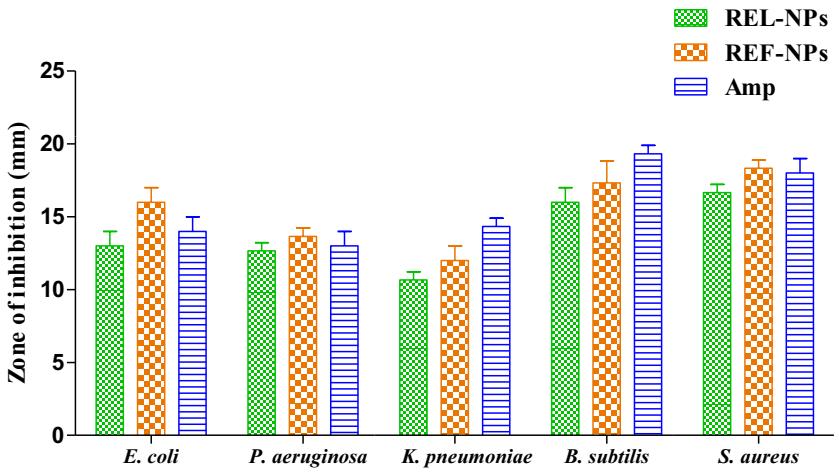

Fig. 15 Antibacterial activity of REL-NPs and REF-NPs against Gram-positive and Gram-negative bacteria

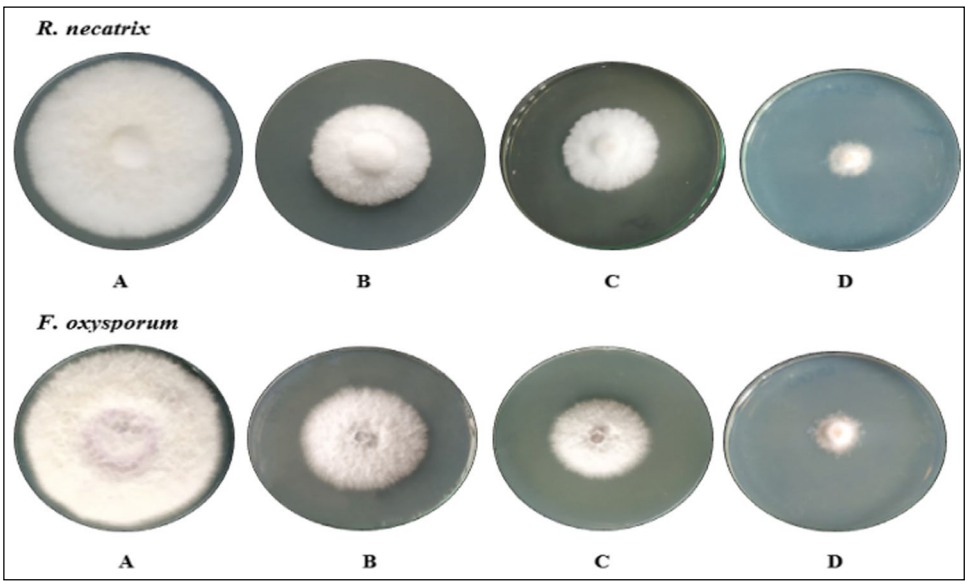

Fig. 16 Petriplates showing the percentage inhibition of REL-NPs and REF-NPs against *F. oxysporum* and *R. necatrix* [A *R. necatrix* and *F. oxysporum* control (without extract and nanoparticles), B REL-NPs (2 mg/mL), C REF-NPs (2 mg/mL), and D positive control (Hyg: 0.1 mg/mL)

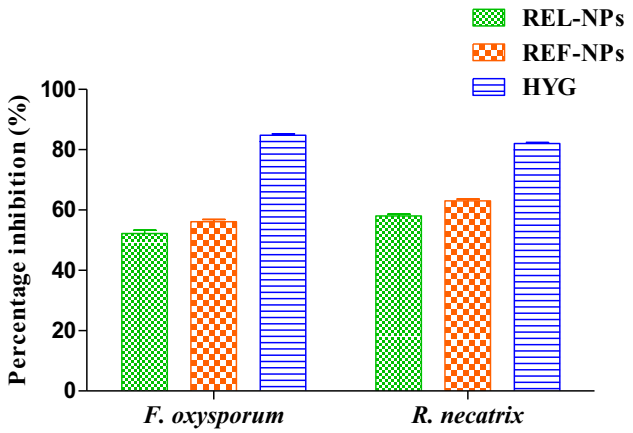

Fig. 17 Antifungal activity of REL-NPs and REF-NPs against fungi

Table 3 MIC of REL-NPs and REF-NPs against bacterial and fungal strains

Microbial strains	MIC (µg/mL)		
	REL-NPs	REF-NPs	Positive control
E. coli	500	500	6.2
P. aeruginosa	1000	500	6.2
K. pneumoniae	1000	500	6.2
B. subtilis	250	125	1.5
S. aureus	250	125	3.1
F. oxysporum	500	250	6.2
R. nectatrix	250	125	12.5

(63.0±0.6%; 125 µg/mL) than *F. oxysporum* (56.1±0.7%; 250 µg/mL). Among both nanoparticles, REF-NPs had higher antifungal potential than RFL-NPs, as revealed with lower MIC values. The lower MIC value indicated higher antifungal potential, as in Table 3. In the previous study, the bismuth oxide shows good antifungal activity against *Candida* species [82, 83]. Oxygen molecules present on the surface of nanoparticles could be responsible for killing microorganisms [84].

The antimicrobial mechanism of inorganic compounds has yet to be understood, and their specific action method against bacteria and fungi still needs to be fully elucidated (Fig. 18). Nanoparticles release metal ions, allowing electrostatic contact between negatively charged cell membranes and positively charged nanoparticles. The production of ROS (reactive oxygen species) plays a crucial role in antimicrobial activity. The Singlet oxygen, OH radicals, and H_2O_2 all play significant roles in the mechanism, including alteration of enzymes and proteins, DNA damage, and causes membrane disruption [85].

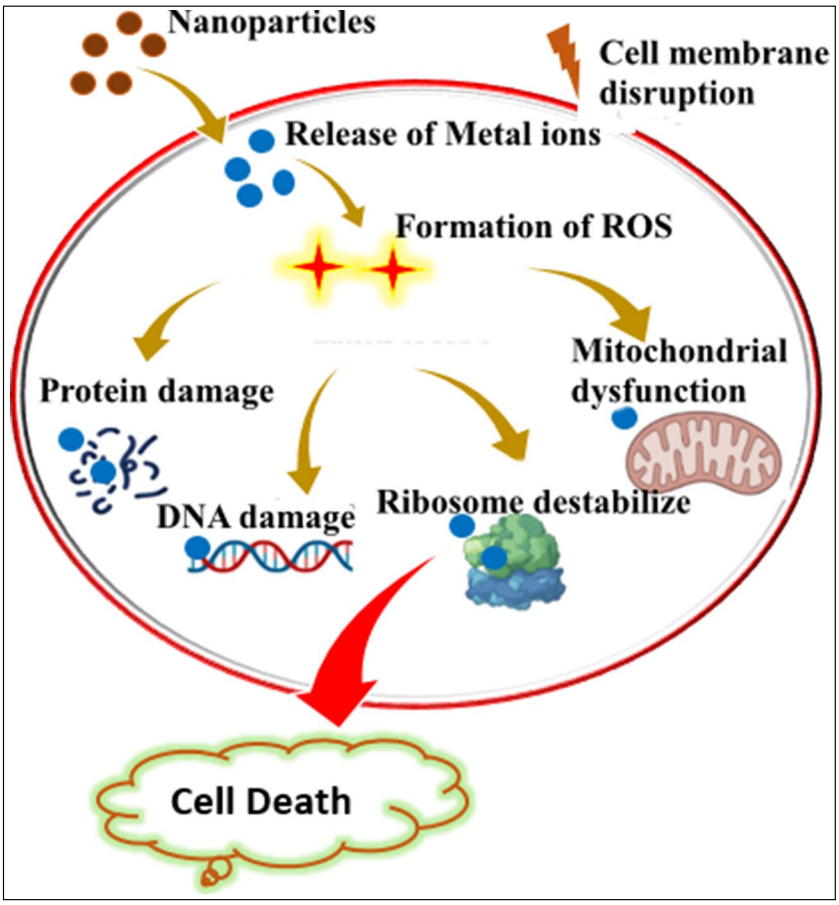

Fig. 18 Probable mechanism of antimicrobial action using nanoparticles

5 Conclusion

The current study demonstrates the green synthesis of α-Bi_2O_3 NPs utilizing leaves and fruit extracts of *R. ellipticus*. The crystal structure, shape, and optical properties of the α-Bi_2O_3 NPs were also comprehensively investigated. REF-NPs and REL-NPs were tested for the visible light photocatalytic degradation of the hazardous Congo red dye. The photocatalytic performance of REF-NPs and REL-NPs was found with photodegradation efficiency of 84.2% for REF-NPs and 89.2% for REL-NPs. Compared to the REF-NPs sample, REL-NPs had the highest rate, which was found to be 1.4 times higher. Photodegradation studies demonstrated that the plant extract-based green Bi_2O_3 had improved Congo red dye degradation ability. Compared with REL-NPs, REF-NPs displayed higher antioxidant activity, which could be attributed to the higher ascorbic content in the fruits of *R. ellipticus* than in the leaves. Additionally, REL-NPs and REF-NPs displayed higher antimicrobial potential against Gram-positive bacteria than Gram-negative bacteria, possibly due to more phytocompounds. The current study presents a straightforward green technique for fabricating innovative α-Bi_2O_3 as a spectacular nanomaterial for aquatic bodies to break down dangerous contaminants via visible light photo-degradation and an antibacterial agent. This study would also motivate others to use bismuth-based nanomaterials and a practical strategy to building-wide band gap bismuth-based photocatalysts for efficient visible light photo-degradation in environmental remediation as well as biomedical applications.

Author contributions Ankush Chauhan and Ritesh Verma designed the study and written the manuscript; Jyoti Dhatwalia, Manpreet Kaur, and Janani Vignesh collected plant samples, synthesized, and characterized the nano-materials; Vishal Dutta and Gopalakrishnan Chandrasekaran were involved in the interpretation of data; Amita Kumari, Suresh Ghotekar, and Shabnam Thakur reviewed the literature and conducted antimicrobial and photocatalytic studies.

Data availability The manuscript includes all data obtained during conducting the research. Data will be made available on request.

Declarations

Ethical approval Not applicable

Competing interests The authors declare no competing interests.

References

1. Majedul Islam M (2022) Threats to humanity from climate change, in: Climate Change. In: The Social and Scientific Construct. Springer, pp 21–36. https://doi.org/10.1007/978-3-030-86290-9_2
2. Abbass K, Qasim MZ, Song H, Murshed M, Mahmood H, Younis I (2022) A review of the global climate change impacts, adaptation, and sustainable mitigation measures. Environ Sci Pollut Res 29:42539–42559. https://doi.org/10.1007/s11356-022-19718-6
3. Chinemerem Nwobodo D, Ugwu MC, Oliseloke Anie C, Al-Ouqaili MT, Chinedu Ikem J, Victor Chigozie U, Saki M (2022) Antibiotic resistance: the challenges and some emerging strategies for tackling a global menace. J Clin Lab Anal 36:e24655. https://doi.org/10.1002/jcla.24655
4. Murray CJ, Ikuta KS, Sharara F, Swetschinski L, Aguilar GR, Gray A, Han C, Bisignano C, Rao P, Wool E (2019) Global burden of bacterial antimicrobial resistance in : a systematic analysis. The Lancet 399(2022):629–655. https://doi.org/10.1016/S0140-6736(21)02724-0
5. Dadgostar P (2019) Antimicrobial resistance: implications and costs. Infect Drug Resist:3903–3910. https://doi.org/10.2147/IDR.S234610
6. Kumar A, Gora MK, Lal G, Choudhary BL, Meena PL, Dhaka RS, Singhal RK, Kumar S, Dolia SN (2023) Impact of Gd3+ doping on structural, electronic, magnetic, and photocatalytic properties of MnFe2O4 nanoferrites and application in dye-polluted wastewater remediation. Environ Sci Pollut Res 30:18820–18842. https://doi.org/10.1007/s11356-022-23420-y
7. Meena PL, Poswal K, Surela AK, Saini JK (2023) Synthesis of graphitic carbon nitride/zinc oxide (g-C3N4/ZnO) hybrid nanostructures and investigation of the effect of ZnO on the photodegradation activity of g-C3N4 against the brilliant cresyl blue (BCB) dye under visible light irradiation. Advanc Composit Hybrid Mater 6:16. https://doi.org/10.1007/s42114-022-00577-1
8. Meena PL, Poswal K, Surela AK (2022) Facile synthesis of ZnO nanoparticles for the effective photodegradation of malachite green dye in aqueous solution. Water Environ J 36:513–524. https://doi.org/10.1111/wej.12783
9. Al-Tohamy R, Ali SS, Li F, Okasha KM, Mahmoud YA-G, Elsamahy T, Jiao H, Fu Y, Sun J (2022) A critical review on the treatment of dye-containing wastewater: ecotoxicological and health concerns of textile dyes and possible remediation approaches for environmental safety. Ecotoxicology and Environmental Safety 231:113160. https://doi.org/10.1016/j.ecoenv.2021.113160
10. Balarabe BY, Bowmik S, Ghosh A, Maity P (2022) Photocatalytic dye degradation by magnetic XFe2O3 (X: Co, Zn, Cr, Sr, Ni, Cu, Ba, Bi, and Mn) nanocomposites under visible light: a cost efficiency comparison. J Magnet Magnet Mater 562:169823. https://doi.org/10.1016/j.jmmm.2022.169823
11. Balarabe BY, Maity P (2022) Visible light-driven complete photocatalytic oxidation of organic dye by plasmonic Au-TiO2 nanocatalyst under batch and continuous flow condition. Colloids Surfaces A: Physicochem Eng Aspects 655:130247. https://doi.org/10.1016/j.colsurfa.2022.130247
12. Yaou Balarabe B, Illiassou Oumarou MN, Koroney AS, Adjama I, Ibrahim Baraze AR (2023) Photo-oxidation of organic dye by Fe 2 O 3 nanoparticles: catalyst, electron acceptor, and polyurethane membrane (PU-Fe 2 O 3) effects. J Nanotech 2023. https://doi.org/10.1155/2023/1292762
13. Meena PL, Poswal K, Surela AK, Saini JK (2021) Facile synthesis of ZnO/CuO/Ag2O ternary metal oxide nanocomposite for effective photodegradation of organic water pollutants. Water Sci Technol 84:2615–2634. https://doi.org/10.2166/wst.2021.431
14. Harja M, Buema G, Bucur D (2022) Recent advances in removal of Congo Red dye by adsorption using an industrial waste. Sci Rep 12:6087. https://doi.org/10.1038/s41598-022-10093-3
15. Karaman C, Karaman O, Show P-L, Karimi-Maleh H, Zare N (2022) Congo red dye removal from aqueous environment by cationic surfactant modified-biomass derived carbon: equilibrium, kinetic, and thermodynamic modeling, and forecasting via

artificial neural network approach. Chemosphere 290:133346. https://doi.org/10.1016/j.chemosphere.2021.133346
16. Kaushik J, Kumar V, Tripathi KM, Sonkar SK (2022) Sunlight-promoted photodegradation of Congo red by cadmium-sulfide decorated graphene aerogel. Chemosphere 287:132225. https://doi.org/10.1016/j.chemosphere.2021.132225
17. Hitkari G, Chowdhary P, Kumar V, Singh S, Motghare A (2022) Potential of copper-zinc oxide nanocomposite for photocatalytic degradation of congo red dye. Clean Chem Eng 1:100003. https://doi.org/10.1016/j.clce.2022.100003
18. Sun J, Chen X, Mo S, Zhang Z, Guo D, Li Y, Liu L (2022) Recent advances of bismuth halide based nanomaterials for photocatalytic antibacterial and photodynamic therapy. Advan Mater Inter 9:2200704. https://doi.org/10.1002/admi.202200704
19. Prakash M, Kavitha HP, Abinaya S, Vennila JP, Lohita D (2022) Green synthesis of bismuth based nanoparticles and its applications-a review. Sustain Chem Phar 25:100547. https://doi.org/10.1016/j.scp.2021.100547
20. Raghunath A, Perumal E (2017) Metal oxide nanoparticles as antimicrobial agents: a promise for the future. Int J Antimicro Agent 49:137–152. https://doi.org/10.1016/j.ijantimicag.2016.11.011
21. Modena MM, Rühle B, Burg TP, Wuttke S (2019) Nanoparticle characterization: what to measure? Advanc Mater 31:1901556. https://doi.org/10.1002/adma.201901556
22. Schrand AM, Rahman MF, Hussain SM, Schlager JJ, Smith DA, Syed AF (2010) Metal-based nanoparticles and their toxicity assessment. Wiley Interdiscip rev: Nanomed Nanobiotech 2:544–568. https://doi.org/10.1002/wnan.103
23. Sabouri Z, Sabouri M, Amiri MS, Khatami M, Darroudi M (2022) Plant-based synthesis of cerium oxide nanoparticles using Rheum turkestanicum extract and evaluation of their cytotoxicity and photocatalytic properties. Mater Techn 37:555–568. https://doi.org/10.1080/10667857.2020.1863573
24. Joudeh N, Linke D (2022) Nanoparticle classification, physicochemical properties, characterization, and applications: a comprehensive review for biologists. J Nanobiotech 20:262. https://doi.org/10.1186/s12951-022-01477-8
25. Meena PL, Poswal K, Surela AK, Meena KS, Mordhiya B (2023) Ag2O-adorned ZnO nanostructures: cooperative and sustainable nanomaterial system for effective reduction and mineralization of hazardous water pollutants. Environ Sci Pollut Res 30:68770–68791. https://doi.org/10.1007/s11356-023-27215-7
26. Sabouri Z, Sabouri S, Moghaddas SSTH, Mostafapour A, Gheibihayat SM, Darroudi M (2022) Plant-based synthesis of Ag-doped ZnO/MgO nanocomposites using Caccinia macranthera extract and evaluation of their photocatalytic activity, cytotoxicity, and potential application as a novel sensor for detection of Pb2+ ions. Biomass Convers Biorefin:1–13. https://doi.org/10.1007/s13399-022-02907-1
27. Meng X, Zhang Z (2016) Bismuth-based photocatalytic semiconductors: introduction, challenges and possible approaches. J Mole Cataly A: Chem 423:533–549. https://doi.org/10.1016/j.molcata.2016.07.030
28. Jalalah M, Faisal M, Bouzid H, Park J-G, Al-Sayari S, Ismail AA (2015) Comparative study on photocatalytic performances of crystalline α-and β-Bi2O3 nanoparticles under visible light. J Indust Eng Chem 30:183–189. https://doi.org/10.1016/j.jiec.2015.05.020
29. Huang X, Zhang W, Tan Y, Wu J, Gao Y, Tang B (2016) Facile synthesis of rod-like Bi2O3 nanoparticles as an electrode material for pseudocapacitors. Ceram Int 42:2099–2105. https://doi.org/10.1016/j.ceramint.2015.09.157
30. Fang W, Zhang N, Fan L, Sun K (2016) Bi2O3 nanoparticles encapsulated by three-dimensional porous nitrogen-doped graphene for high-rate lithium ion batteries. J Pow Sour 333:30–36. https://doi.org/10.1016/j.jpowsour.2016.09.155
31. Nayef UM, Kamel RI (2020) Bi2O3 nanoparticles ablated on porous silicon for sensing NO2 gas. Optik 208:164146. https://doi.org/10.1016/j.ijleo.2019.164146
32. Ahamed M, Akhtar MJ, Khan MM, Alrokayan SA, Alhadlaq HA (2019) Oxidative stress mediated cytotoxicity and apoptosis response of bismuth oxide (Bi2O3) nanoparticles in human breast cancer (MCF-7) cells. Chemosphere 216:823–831. https://doi.org/10.1016/j.chemosphere.2018.10.214
33. Miao CC, Yuan GQ (2018) Morphology-controlled Bi2O3 nanoparticles as catalysts for selective electrochemical reduction of CO2 to formate. Chem Electro Chem 5:3741–3747. https://doi.org/10.1002/celc.201801036
34. Oudghiri-Hassani H, Rakass S, Al Wadaani FT, Al-Ghamdi KJ, Omer A, Messali M, Abboudi M (2015) Synthesis, characterization and photocatalytic activity of α-Bi2O3 nanoparticles, Journal of Taibah University for. Science 9:508–512. https://doi.org/10.1016/j.jtusci.2015.01.009
35. Kamel RI, Ahmed DS, Nayef UM (2019) Synthesis of Bi2O3 nanoparticles by laser ablation on porous silicon for photoconversion application. Optik 193:163013. https://doi.org/10.1016/j.ijleo.2019.163013
36. Huang Q, Zhang S, Cai C, Zhou B (2011) β-and α-Bi2O3 nanoparticles synthesized via microwave-assisted method and their photocatalytic activity towards the degradation of rhodamine B. Mater Lett 65:988–990. https://doi.org/10.1016/j.matlet.2010.12.055
37. Malligavathy M, Pathinettam Padiyan D (2021) Role of pH in the hydrothermal synthesis of phase pure alpha Bi2O3 nanoparticles and its structural characterization. Advan Mater Proceed 2:51–55. https://doi.org/10.5185/amp.2017/112
38. Varshney A, Khan JA, Ahmad I, Uddin I (2021) Room temperature chemical synthesis of Bi2O3 nanoparticles. Micro & Nano Lett 16:509–514. https://doi.org/10.1049/mna2.12077
39. Hernández-Díaz JA, Garza-García JJ, Zamudio-Ojeda A, León-Morales JM, López-Velázquez JC, García-Morales S (2021) Plant-mediated synthesis of nanoparticles and their antimicrobial activity against phytopathogens. J Sci Food Agri 101:1270–1287. https://doi.org/10.1002/jsfa.10767
40. Ali J, Ali N, Wang L, Waseem H, Pan G (2019) Revisiting the mechanistic pathways for bacterial mediated synthesis of noble metal nanoparticles. J Microbiol Methods 159:18–25. https://doi.org/10.1016/j.mimet.2019.02.010
41. Sabouri Z, Oskuee RK, Sabouri S, Moghaddas SSTH, Samarghandian S, Abdulabbas HS, Darroudi M (2023) Phytoextract-mediated synthesis of Ag-doped ZnO–MgO–CaO nanocomposite using Ocimum Basilicum L seeds extract as a highly efficient photocatalyst and evaluation of their biological effects. Ceram Int 49:20989–20997. https://doi.org/10.1016/j.ceramint.2023.03.234
42. Sabouri Z, Sabouri S, Tabrizi SS, Moghaddas H, Mostafapour A, Amiri MS, Darroudi M (2022) Facile green synthesis of Ag-doped ZnO/CaO nanocomposites with Caccinia macranthera seed extract and assessment of their cytotoxicity, antibacterial, and photocatalytic activity. Bioprocess Biosyst Eng 45:1799–1809. https://doi.org/10.1007/s00449-022-02786-w
43. Gour A, Jain NK (2019) Advances in green synthesis of nanoparticles. Artifi cells, nanomed, biotech 47:844–851. https://doi.org/10.1080/21691401.2019.1577878
44. Trivedi A, Verma S, Arya R, Mehta P, Tyagi R (2014) Variability in vegetative characters and yield attributes of Raspberry (Rubus spp.) in Uttarakhand Himalayas. Int J Fruit Sci 14:107–116. https://doi.org/10.1080/15538362.2013.817774
45. Khaniya L, Bhattarai R, Jan HA, Hussain W, Abbasi AM, Bussmann RW, Paniagua-Zambrana NY (2021) Rubus ellipticus Sm. In: Rubus foliolosus Weihe & Nees Rubus fruticosus L. Rubus irritans Focke Rosaceae, in: Ethnobotany of the Himalayas.

Springer, pp 1717–1733. https://doi.org/10.1007/978-3-030-57408-6_208
46. Rojas-Vera J, Patel AV, Dacke CG (2002) Relaxant activity of raspberry (Rubus idaeus) leaf extract in guinea-pig ileum in vitro. Phytother Res: An Int J Devoted Pharma Toxicol Evaluation Nat Prod Deriv 16:665–668. https://doi.org/10.1002/ptr.1040
47. Tripathi AN, Kumar P, Sati SC (2020) Uses of invasive alien plants in Kumaun Himalayan folk medicinal system. Int J Herb Med 8:27–31
48. Rokaya MB, Münzbergová Z, Timsina B (2010) Ethnobotanical study of medicinal plants from the Humla district of western Nepal. J Ethnopharma 130:485–504. https://doi.org/10.1016/j.jep.2010.05.036
49. Badhani A, Rawat S, Bhatt ID, Rawal RS (2015) Variation in chemical constituents and antioxidant activity in Yellow Himalayan (Rubus ellipticus Smith) and Hill Raspberry (Rubus niveus Thunb.). J Food Biochem 39:663–672. https://doi.org/10.1111/jfbc.12172
50. Kewlani P, Tiwari D, Rawat S, Bhatt ID (2022) Pharmacological and phytochemical potential of Rubus ellipticus: a wild edible with multiple health benefits. J Pharma Pharma. https://doi.org/10.1093/jpp/rgac053
51. Meena PL, Surela AK, Saini JK, Chhachhia LK (2022) Millettia pinnata plant pod extract-mediated synthesis of Bi2O3 for degradation of water pollutants. Environ Sci Pollut Res 29:79253–79271. https://doi.org/10.1007/s11356-022-21435-z
52. Meena PL, Surela AK, Poswal K, Saini JK, Chhachhia LK (2022) Biogenic synthesis of Bi2O3 nanoparticles using Cassia fistula plant pod extract for the effective degradation of organic dyes in aqueous medium. Biomass Convers Biorefin:1–17. https://doi.org/10.1007/s13399-022-02605-y
53. Motakef-Kazemi N, Yaqoubi M (2020) Green synthesis and characterization of bismuth oxide nanoparticle using mentha pulegium extract. Iranian J Pharma Res: IJPR 19:70. https://doi.org/10.22037/ijpr.2019.15578.13190
54. Nurmalasari N, Yulizar Y, Apriandanu D (2020) Bi2O3 nanoparticles: synthesis, characterizations, and photocatalytic activity. In: IOP Conference Series: Materials Science and Engineering. IOP Publishing, p 012036. https://doi.org/10.1088/1757-899X/763/1/012036
55. Rao RP, Mishra S, Tripathi R, Jain SK (2021) Bismuth oxide nanorods: phytochemical mediated one-pot synthesis and growth mechanism. Inorganic Nano-Metal Chem:1–8. https://doi.org/10.1080/24701556.2021.1980037
56. Dhiman P, Rana G, Kumar A, Dawi EA, Sharma G (2023) Rare earth doped ZnO nanoparticles as spintronics and photo catalyst for degradation of pollutants. Molecules 28:2838. https://doi.org/10.3390/molecules28062838
57. Mishra K, Ojha H, Chaudhury NK (2012) Estimation of antiradical properties of antioxidants using DPPH assay: a critical review and results. Food Chem 130:1036–1043. https://doi.org/10.1016/j.foodchem.2011.07.127
58. Dhatwalia J, Kumari A, Chauhan A, Mansi K, Thakur S, Saini RV, Guleria I, Lal S, Kumar A, Batoo KM (2022) Rubus ellipticus Sm. fruit extract mediated zinc oxide nanoparticles: a green approach for dye degradation and biomedical applications. Materials 15:3470. https://doi.org/10.3390/ma15103470
59. Malmros G (1970) The crystal structure of a-Bi2O3. Acta Chem. Scand 24:384
60. Bokuniaeva A, Vorokh A (2019) Estimation of particle size using the Debye equation and the Scherrer formula for polyphasic TiO2 powder. In: in: journal of physics: Conference series. IOP Publishing, p 012057. https://doi.org/10.1088/1742-6596/1410/1/012057
61. Khairnar SD, Shrivastava VS (2019) Photocatalytic degradation of chlorpyrifos and methylene blue using α-Bi 2 O 3 nanoparticles fabricated by sol–gel method. SN Applied Sciences 1:1–10. https://doi.org/10.1007/s42452-019-0761-4
62. Viruthagiri G, Kannan P, Indhumathi V (2017) Photocatalytic activity of α-phase bismuth oxide nanoparticles under visible light. Int J Advanc Sci Res 2:1–7
63. Raza W, Haque M, Muneer M, Harada T, Matsumura M (2015) Synthesis, characterization and photocatalytic performance of visible light induced bismuth oxide nanoparticle. J Alloys Comp 648:641–650. https://doi.org/10.1016/j.jallcom.2015.06.245
64. La J, Huang Y, Luo G, Lai J, Liu C, Chu G (2013) Synthesis of bismuth oxide nanoparticles by solution combustion method. Particulate Sci Technol 31:287–290. https://doi.org/10.1080/02726351.2012.727525
65. Huízar-Félix A, Hernández T, De la Parra S, Ibarra J, Kharisov B (2012) Sol–gel based Pechini method synthesis and characterization of Sm1− xCaxFeO3 perovskite 0.1≤ x≤ 0.5. Powder techn 229:290–293. https://doi.org/10.1016/j.powtec.2012.06.057
66. Mei J, Liao T, Ayoko GA, Sun Z (2019) Two-dimensional bismuth oxide heterostructured nanosheets for lithium-and sodium-ion storages. ACS appl mater inter 11:28205–28212. https://doi.org/10.1021/acsami.9b09882
67. Guan H, Zhang X, Xie Y (2014) Soft-chemical synthetic non-stoichiometric Bi2O2. 33 nanoflower: a new room-temperature ferromagnetic semiconductor. J Phys Chem C 118:27170–27174. https://doi.org/10.1021/jp509045d
68. Köhler R, Ohms G, Militz H, Viöl W (2018) Atmospheric pressure plasma coating of bismuth oxide circular droplets. Coatings 8:312. https://doi.org/10.3390/coatings8090312
69. Chauhan A, Verma R, Batoo KM, Kumari S, Kalia R, Kumar R, Hadi M, Raslan EH, Imran A (2021) Structural and optical properties of copper oxide nanoparticles: a study of variation in structure and antibiotic activity. J Mater Res 36:1496–1509. https://doi.org/10.1557/s43578-021-00193-7
70. Jubu P, Yam F, Igba V, Beh K (2020) Tauc-plot scale and extrapolation effect on bandgap estimation from UV–vis–NIR data–a case study of β-Ga2O3. Journal of Solid State Chemistry 290:121576. https://doi.org/10.1016/j.jssc.2020.121576
71. Balarabe BY, Paria S, Keita DS, Baraze ARI, Kalugendo E, Tetteh GNT, Meringo MM, Oumarou MNI (2022) Enhanced UV-light active α-Bi2O3 nanoparticles for the removal of methyl orange and ciprofloxacin. Inorganic Chem Commun 146:110204. https://doi.org/10.1016/j.inoche.2022.110204
72. Dutta V, Sharma S, Raizada P, Kumar R, Thakur VK, Nguyen V-H, Asiri AM, Khan AAP, Singh P (2020) Recent progress on bismuth-based Z-scheme semiconductor photocatalysts for energy and environmental applications. J Environ Chem Eng 8:104505. https://doi.org/10.1016/j.jece.2020.104505
73. Dutta V, Sonu S, Raizada P, Thakur VK, Ahamad T, Thakur S, Kumar Verma P, Quang HHP, Nguyen V-H, Singh P (2022) Prism-like integrated Bi2WO6 with Ag-CuBi2O4 on carbon nanotubes (CNTs) as an efficient and robust S-scheme interfacial charge transfer photocatalyst for the removal of organic pollutants from wastewater. Environ Sci Pollut Res:1–16. https://doi.org/10.1007/s11356-022-20743-8
74. Saklani S, Chandra S, Badoni P, Dogra S (2012) Antimicrobial activity, nutritional profile and phytochemical screening of wild edible fruit of Rubus ellipticus. Int J Med Aromat Plants 2:269–274
75. Shibu Prasanth S, Chandran P (2017) Phytochemical and antimicrobial analysis of leaf samples of different Rubus species. Intl J Chem Tech Res 10:359–368
76. Moharekar S, Raskar P, Wani A, Moharekar S (2014) Synthesis and comparative study of zinc oxide nanoparticles with and without capping of pectin and its application, World. J Pharm Pharm Sci 3:1255–1267

77. Ramesh P, Saravanan K, Manogar P, Johnson J, Vinoth E, Mayakannan M (2021) Green synthesis and characterization of biocompatible zinc oxide nanoparticles and evaluation of its antibacterial potential. Sensing and Bio-Sensing Research 31:100399. https://doi.org/10.1016/j.sbsr.2021.100399
78. Shakibaie M, Amiri-Moghadam P, Ghazanfari M, Adeli-Sardou M, Jafari M, Forootanfar H (2018) Cytotoxic and antioxidant activity of the biogenic bismuth nanoparticles produced by Delftia sp. SFG, Materials Research Bulletin 104:155–163. https://doi.org/10.1016/j.materresbull.2018.04.001
79. Das PE, Majdalawieh AF, Abu-Yousef IA, Narasimhan S, Poltronieri P (2020) Use of a hydroalcoholic extract of Moringa oleifera leaves for the green synthesis of bismuth nanoparticles and evaluation of their anti-microbial and antioxidant activities. Materials 13:876. https://doi.org/10.3390/ma13040876
80. Qasim S, Zafar A, Saif MS, Ali Z, Nazar M, Waqas M, Haq AU, Tariq T, Hassan SG, Iqbal F (2020) Green synthesis of iron oxide nanorods using Withania coagulans extract improved photocatalytic degradation and antimicrobial activity. J Photochem Photobiol B: Biol 204:111784. https://doi.org/10.1016/j.jphotobiol.2020.111784
81. Jassim AM, Farhan SA, Salman JA, Khalaf KJ, Al Marjani MF, Mohammed MT (2015) Study the antibacterial effect of bismuth oxide and tellurium nanoparticles. Int j chem biol sci 1:81–84
82. Hernandez-Delgadillo R, Velasco-Arias D, Martinez-Sanmiguel JJ, Diaz D, Zumeta-Dube I, Arevalo-Niño K, Cabral-Romero C (2013) Bismuth oxide aqueous colloidal nanoparticles inhibit Candida albicans growth and biofilm formation. Int J Nanomed:1645–1652. https://doi.org/10.2147/IJN.S38708
83. Indurkar AR, Sangoi VD, Patil PB, Nimbalkar MS (2018) Rapid synthesis of Bi2 O3 nano-needles via 'green route'and evaluation of its anti-fungal activity. IET Nanobiotech 12:496–499. https://doi.org/10.1049/iet-nbt.2017.0070
84. Król A, Pomastowski P, Rafińska K, Railean-Plugaru V, Buszewski B (2017) Zinc oxide nanoparticles: synthesis, antiseptic activity and toxicity mechanism. Advances Coll Interf Sci 249:37–52. https://doi.org/10.1016/j.cis.2017.07.033
85. Ali MA, Fahad S, Haider I, Ahmed N, Ahmad S, Hussain S, Arshad M (2019) Oxidative stress and antioxidant defense in plants exposed to metal/metalloid toxicity, Reactive Oxygen, Nitrogen and Sulfur Species in Plants: Production, Metabolism. Signaling Defense Mechan:353–370. https://doi.org/10.1002/9781119468677.ch15